Electronic Supplementary Material (ESI) for CrystEngComm.

Supporting Information

Where the extraordinaries meet: a cascade of isosymmetrical superionic phase transitions and negative thermal expansion in a novel silver salt-inclusion borate halide

Sergey N. Volkov*, Dmitri O. Charkin, Maxim Yu. Arsent'ev, Sergey M. Aksenov, Lev S. Manelis, Maria G. Krzhizhanovskaya, Olga Yu. Sinel'shchikova, Valery L. Ugolkov, Alexey V. Povolotskiy, Vladimir V. Shilovskikh, Andrey A. Antonov, and Rimma S. Bubnova

Table of Contents

A. Experimental Procedures

1.1. Reagents

H_3BO_3 (NevaReaktiv, Russia, 99.8 %), $AgNO_3$ (Lenreactiv, Russia, 99.0 %), KI (Reakhim, Russia, 99.0 %) and NaI*2H_2O (Reakhim, Russia, 99.0 %) were used as received. Phase identification of the prepared samples was carried out using a Rigaku Miniflex II (30 kV/10 mA) diffractometers utilizing Co Kα radiation ($\lambda_{K\alpha1}$ = 1.78897 Å, $\lambda_{K\alpha2}$ = 1.79285 Å).

1.2. Synthesis

Single crystals of $Ag_3B_6O_{10}I$ were initially obtained by glass crystallization, a 1:1 mixture of AgI (prepared by precipitation from $AgNO_3$ and KI solutions), and "$Ag_2B_4O_7$" precursor prepared as described in [1] was placed into a silica-jacketed platinum crucible, evacuated, sealed, and annealed at 800 °C with slow cooling to 450 °C. The dark transparent glass was gently broken into pieces of 1−2 mm and annealed in evacuated silica capsules at 450 °C for one month.

A bulk sample was prepared by annealing a 1:2 mixture of AgI and "AgB_3O_5" precursor (prepared by stepwise heating $AgNO_3$ and boric acid in 1:3 molar ratio in evacuated silica capsules at 400 and 450 °C for one week at each step, with intermediate grinding. A small admixture of AgI was detected.

The sample containing crystals of $Na_3B_6O_{10}I$ was prepared the same way as $Ag_3B_6O_{10}I$ starting from NaI (obtained via decomposition of dihydrate at 150 °C in a dynamic vacuum, to prevent oxidation) and $Na_2B_4O_7$ (prepared by slow heating of borax). The obtained sample was a mixture of NaI (5 wt %), NaI*2H_2O (25 wt %), NaB_3O_5 (63 %), and $Na_3B_6O_{10}I$ (7 %)

1.3. X-ray Powder Diffraction

A Rietveld refinement was performed for $Ag_3B_6O_{10}I$, to check the consistency between the single crystal and powder sample used for the properties study. The final structure model of $Ag_3B_6O_{10}I$ obtained from single-crystal data (see below) was used in the refinement utilizing RietveldToTensor software.[2] Final Rietveld refinement results are presented in Table S37. They show good agreement with the single−crystal data. The final refinement resulted in values R_{wp} = 0.060, R_{Bragg} = 0.033 for $Ag_3B_6O_{10}I$. The lattice parameters obtained from the powder diffraction data are in good agreement with those derived from the single-crystal data. Pseudo-Voigt functions were used for fitting the reflection profiles. The background was described by a Chebyshev polynomial function (31st order). The atomic coordinates and anisotropic displacement parameters were refined only for silver and iodine atoms. The final Rietveld refinement plot is given in Figure S3.

1.4. Single−crystal X-ray analysis and crystal structure solution

Single crystal of $Ag_3B_6O_{10}I$ (0.084×0.122×0.276 mm) and $Na_3B_6O_{10}I$ (0.107×0.162×0.175 mm) were selected in polarized light using an optical microscope and attached to a glass fiber using epoxy glue (Figure S2). The experimental data were collected on a Bruker Apex II diffractometer utilizing Mo *K*α radiation at 25 °C ($Ag_3B_6O_{10}I$ and $Na_3B_6O_{10}I$). High-temperature X-ray single-crystal measurements of ($Ag_3B_6O_{10}I$ were collected on a Rigaku XtaLAB Synergy-S four-circle diffractometer utilizing Mo *K*α radiation at 110, 120, 140, 300 and 400 °C. A hot air blower (FMB Oxford, UK) was used for temperature control. Lorentz and polarization corrections were applied. The absorption correction based on a crystal shape was performed for room-temperature measurement. At high temperatures, the crystal was placed inside the quartz capillary and we were unable to correctly determine its shape. As a result, a multi-scan absorption correction[3] for temperature-dependent studies. An isotropic extinction-correction did not improve the refinement for all crystals. A trial refinement including a Becker-Coppens type I parameter for isotropic extinction neither yielded a significant value with $g_{iso} > 3\sigma[g_{iso}]$. So extinction correction was not applied for all measurements. The observed Laue symmetry and systematic absences were indicative of the space groups *Pnma* or *Pn*2_1*a*. The centrosymmetric *Pnma* was assumed, and subsequent refinements confirmed the choice of this space group. The structures were solved using a charge-flipping method[4] implemented in JANA2006 [5]. Data visualization was performed with the Vesta[6] and Atoms 6.1 software.[7]

Initially, 2 Ag, 1 I, 6 O, and 4 B sites were localized for $Ag_3B_6O_{10}I$, and 3 Na, 1 I, 6 O, and 4 B atom sites were localized for $Na_3B_6O_{10}I$. All atoms were refined in anisotropic approximation resulting in R_{obs} of 0.083 for 1 and 0.028 for 2. The attained structure model for $Ag_3B_6O_{10}I$ rather poorly described the observed distribution of electron density in the vicinity of silver and iodine sites as clearly illustrated by the difference electron density maps (Figure S11). Therein, significant residual electron-density maxima and minima of 10.39/–6.83 e Å^{-3} remained unaccounted. Therefore, an anharmonic refinement of silver sited was performed starting from the anisotropic structural model. The joint-probability density function was calculated from the inverse Fourier transform of the anharmonic ADPs approximated by the high−order expansion of the Gram−Charlier series [8,9].

At the first step, the silver and iodine atoms were refined using anharmonic coefficients of up to 3rd order which resulted in R_{obs} of 0.046 (Figures S11c, f, l). Yet, essential residual electron-density maxima and minima of 4.12/–4.01 e Å^{-3} persisted around Ag2 (Figure S11l). Next, 4th and 5th order anharmonic coefficients were added which permitted to reduce R_{obs} to 0.036 (residual electron-density maxima and minima of 2.52/–2.21 e Å^{-3}) (Figure S11j) and further to 0.031 (residual electron-density maxima and minima of 1.72/–1.41 e Å^{-3}) (Figure S11k). Inspection

of the refined anharmonic coefficients showed that a large part approached zero within the error limits. Thus, 28 out of 58 anharmonic coefficients of the 3rd, 4th, and 5th orders were fixed to zero.

The structural model for the room-temperature phase, *δ*-$Ag_3B_6O_{10}I$ was then employed for refinement of *β*-$Ag_3B_6O_{10}I$ at 110 °C. Analysis of the difference electron density maps revealed three additional Ag3, Ag4, and Ag5 silver sites with occupancy factors of ~0.5, 0.2, and 0.3, respectively. The free refinement of the silver position occupancies showed ~0.68 and 0.34 occupancy factors for Ag1 and Ag2, respectively. Hence, Ag1−Ag5 occupancies were refined with the constraints of the chemical formula of "$Ag_3B_6O_{10}I$". The same refinement was performed for *β*-$Ag_3B_6O_{10}I$ data measured at 120, 140, and 300 °C. The measurement at 400 °C has shown one additional silver site at 4*b* Wyckoff site with ~0.13 occupancy factor. Then the Ag1−Ag6 occupancies were refined with the constraints of the chemical formula.

The order of the anharmonic coefficients used is listed in Table S3. The highest-order ones were employed for refinement of the room-temperature data. At higher temperatures, the sharp increase of thermal motions leads to a decrease in diffraction intensities, which hampers the correct refinement of anharmonic parameters. The main features of the X-ray diffraction experiment and structure refinement are summarized in Tables S1−S34.

1.5. EDX

Energy-dispersive X-ray spectroscopy (EDX) was performed on a Hitachi S3400N scanning electron microscope (SEM) equipped with an Oxford Instruments X-Max 20 Energy Dispersive Spectrometer. The electron-beam accelerating voltage was 20 kV and the current 5 1.8 nA; defocused beam (up to 4 μm spot size) was used and the X-ray acquisition time was 30 s. The chemical composition was measured on different spots on several crystals and eventually averaged. The final composition was normalized to 100 %.

1.6. High-temperature X-ray powder diffraction

Thermal expansion of $Ag_3B_6O_{10}I$ was studied in the air by high-temperature X-ray powder diffraction (HTXRD) data collected using Rigaku Ultima IV X-ray diffractometer (CoKα radiation, 40 kV/30 mA, Bragg–Brentano geometry, PSD D-Tex Ultra) with a high-temperature camera (Rigaku R-300 high-temperature attachment). The samples were prepared on a Pt-Rh plate.

Two experiments were performed to study the reproducibility of the phase transitions. The first was performed at 30−660 °C, while the second contained two cycles in the ranges of 30−300 °C and 30−250 °C. For the first experiment, temperature steps of 20 °C were adopted over the whole 30−660 °C range. For the detailed study of the phase transitions in $Ag_3B_6O_{10}I$, temperature step of 2 °C in the 60–160 °C range was used in the second experiment for both cycles. The step of 10 °C was used for the 30−60 °C and 160−300/160−250 °C (second experiment, first/second cycle, respectively).

Unit cell parameters were refined at different temperatures by the Rietveld method using RietveldToTensor software[2] based on data collected during the second experiment, the second cycle. Pseudo−Voigt functions were used for fitting the reflection profiles. The background was described by a Chebyshev polynomial function (15th order). Temperature dependences of unit−cell parameters and volume (Figure S10) of $Ag_3B_6O_{10}I$ over the whole temperature range can be described by the following equations:

25−80 °C, *δ*-$Ag_3B_6O_{10}I$
$a = 12.74905(100)+0.000082(15)t$
$b = 9.71786(37)−0.0001163(58)t$
$c = 8.42052(65)+0.000107(10)t$
$V = 1043.249(82)+0.0075(13)t$

80−100 °C, *β*-$Ag_3B_6O_{10}I$
$a = 12.7533(35)+0.000037(38)t$
$b = 9.7214(19)−0.000161(20)t$
$c = 8.4129(16)+0.000205(18)t$
$V = 1043.03(40)+0.0112(44)t$

104−120 °C, *β*-$Ag_3B_6O_{10}I$
$a = 12.7383(87) − 0.000068(77)t$
$b = 9.5326(44) − 0.000035(39)t$
$c = 8.5350(30) − 0.000030(27)t$
$V = 1036.41(42) − 0.0131(37)t$

120−250 °C, *α*-$Ag_3B_6O_{10}I$
$a = 12.71197(63) + 0.0001531(38)t$
$b = 9.51505(90) + 0.0000971(55)t$
$c = 8.54194(72) − 0.0000792(44)t$

V = 1033.191(47) + 0.01339(29)t

250−400 °C, α-$Ag_3B_6O_{10}I$
a = 12.7231(27) + 0.0001360(83)t
b = 9.4964(15) + 0.0002059(45)t
c = 8.5516(28) − 0.0001308(86)t
V = 1033.21(45) + 0.0176(14)t

400−600 °C, α-$Ag_3B_6O_{10}I$
a = 12.636(10) + 0.000343(20)t
b = 9.5098(27) + 0.0001749(54)t
c = 8.4691(29) + 0.0000750(57)t
V = 1017.4(1) + 0.0563(21)t

Using the coefficients of approximation, the components of the tensor (Table S35) were determined in a Cartesian crystal-physical coordinate system as the solution of the system of six equations of the following form:
$\alpha_d = \alpha_{11}x_d^2 + \alpha_{22}y_d^2 + \alpha_{33}z_d^2 + 2\alpha_{12}x_dy_d + 2\alpha_{23}y_dz_d + 2\alpha_{13}x_dz_d$, (1)
where α_{ij} are the tensor components and x_d, y_d and z_d are the directional cosines of the normal with respect to the crystal–physical axes xyz.
The thermal expansion along the normal vector to the (hkl) plane with the interplanar distance d_{hkl} is calculated as follows:

$$\alpha_d = \left(\frac{-d_{hkl}^2}{2}\right)\cdot\left(\frac{\partial f}{\partial a}\cdot\frac{da}{dT}+\frac{\partial f}{\partial b}\cdot\frac{db}{dT}+\frac{\partial f}{\partial c}\cdot\frac{dc}{dT}+\frac{\partial f}{\partial \alpha}\cdot\frac{d\alpha}{dT}+\frac{\partial f}{\partial \beta}\cdot\frac{d\beta}{dT}+\frac{\partial f}{\partial \gamma}\cdot\frac{d\gamma}{dT}\right), (2)$$

where f (h, k, l, a, b, c, α, β, γ) is a function of indices and the unit-cell parameters. Standard orientation of the crystallographic axes with respect to the crystal-physical axes has been used. Based on the calculated eigenvalues of the tensor, the surface of the second-rank symmetric tensor or, in other words, the figure of thermal expansion coefficients can be plotted. Each radius vector of this figure represents the value of the thermal expansion coefficient in a certain direction.

1.7. Thermal analysis

DSC and TG studies were performed on NETZSCH STA 409 in a platinum crucible with a heating/cooling rate of 10 °C/min in the range of 20−700 °C. To study the reproducibility of thermal effects, three heating-cooling cycles were performed in the 25−300 °C range (Figure S8). The sample was initially dried at 300 °C. The temperatures of the endothermic effects were estimated as onset temperature which was determined by the DDSC curve.
The discrepancies in the transition temperatures determined by DSC, HTXRPD, and HTXRSD, are most likely due to different heating rates; also, the accuracy of the Pt-Rh/Pt thermocouple is lower in the 25−200 °C region. The DSC data were therefore used as most accurately determined. The entropy change (ΔS) was calculated using the formula $\Delta S = \Delta H/T_C$.

1.8. Impedance spectroscopy

$Ag_3B_6O_{10}I$ impedance spectroscopy was carried out using an Elins-2000 impedance meter in the frequency range from 3 Hz to 2 MHz. Before measurements, electrodes were applied to both parallel surfaces of the samples by firing silver-containing paste at 550 °C. To obtain the temperature dependence of the permittivity, the sample was heated in air to 550 °C, after which the impedance hodograph was recorded for each temperature in the cooling mode. The resistance of the sample was obtained by approximating the high-frequency semicircle to the axis of real values (Figure S23). The data obtained were normalized to the geometric dimensions of the sample. The activation energy was determined from the obtained dependence using the Arrhenius formula.

1.9. Spectroscopy

UV-Vis absorption spectra were measured using a Perkin Elmer Lambda 1050 spectrophotometer equipped with a 150 mm integrated sphere. Barium sulfate ($BaSO_4$) sample was used as a blank. The IR absorption spectra were measured on a Thermo Scientific Nicolet 8700 Fourier spectrometer using an ATR attachment.

1.10. Raman spectroscopy at high temperatures

The temperature dependencies of Raman spectra were measured with a Horiba LabRam spectrometer and Linkam TS1000 heating system. A He-Ne laser with a 632.8 nm wavelength was used to pump the Raman scattering. The laser beam was focused on the powder sample surface by 50× objective with an aperture of 0.5. Raman scattering was collected with the same objective and registered with a resolution of 3 cm^{-1}. The temperature of samples was increased at a rate of 20 °C/min and stabilized for 10 min before every measurement of Raman spectra. The measurements were performed at 30, 40, 50, 60, 70, 80, 90, 100, 110 and 150 °C.

1.11. Computational details

The calculations of $Ag_3B_6O_{10}I$ were performed within the framework of the density−functional theory (DFT) as implemented in the SIESTA 4.0 program package[10] and CASTEP[11]. The exchange-correlation potential within the Generalized Gradient Approximation (GGA) with the Perdew-Burke-Ernzerhof parametrization was used. The core electrons were treated within the frozen core approximation, applying norm-conserving Troullier-Martins pseudopotentials[12] generated using ATOM program (Version 3.2.2)[10].

Geometry optimizations and phonon calculations were performed using norm-conserving pseudopotentials being generated on the fly by CASTEP (OTFG norm-conserving pseudopotentials), Monhorst-Pack mesh 3 x 1 x 3 (4 irreducible k-points), energy cutoff values 898 eV -for $Na_3B_6O_{10}I$, 571 eV - for $Ag_3B_6O_{10}I$. The geometry optimizations were performed using Broyden-Fletcher-Goldfarb-Shanno iterative algorithm (BFGS).[13] A real-space mesh cutoff of 350 Ry and the threshold of 10^{-3} eV were set for the self-consistent field convergence of the total electronic energy. In these atoms, Ag: $5s^14d10$, B: $2s^22p^1$, O: $2s^22p^4$, I: $5s^25p^5$ were treated as valence electrons. The integration of the Brillouin zone was performed by a 4 × 4 × 4 *k*-point grid sampling for density of states, and the Fermi level (E_f = 0 eV) was selected as the reference. For bonding analysis, the crystal orbital Hamilton populations (COHPs)[14] of all filled electronic states for selected atom pairs were calculated. The COHP analyses provide the contributions of the covalent parts of particular pairwise interactions to the total bonding energy of the crystal. The energy-integrated COHP (ICOHP) provides an estimate of the bond energy (the more negative value, the stronger the bonding strength).

1.12. Topological features

The topological features of compounds with the general formula $M_3[B_6O_{10}]X$ (where M = Na, K, Ag; X = Cl^-, I^-) were calculated using the ToposPro software[15]. To perform the topological analysis of the frameworks the cation nets were constructed by transforming the oxygen bridges between cations to the edges of the net, which corresponded to the *standard representation* of the net [16,17]. The topological types of the cation nets were determined by calculating the net topological indices, which unambiguously characterize the net overall topology. To characterize the local topology of the cation net, we constructed natural tilings, which are composed of the smallest polyhedral cationic clusters (natural tiles)[18].

1.13. The Voronoi−Dirichlet partitioning analysis

The Voronoi−Dirichlet partitioning (VDP) analysis of the topology of the Ag^+ migration path was performed using the ToposPro software package. [19] The procedure was described in previous works.[20,21] Algorithms of ToposPro assign Voronoi-Dirichlet polyhedra (VDP) for each atom. The vertexes of such VDPs correspond to the centers of the so-called elementary voids. Around the centers of elementary voids, the VDPs can be built in the same way as for atoms.[20] The radius of the sphere, whose volume is equal to the volume of the VDP void, is designated as the radius of the spherical domain (R_{sd}). The physical sense of the elementary voids means that they correspond to real cavities in the structure or transition regions between the cavities. These voids can form channels, characterized by channel radius (R_{ch}).[22,23] The higher the R_{sd} and R_{ch} values of voids and channels, the more probable is that these voids and channels can be accessible by migrating cation. Using this purely topological approach the migration paths with R_{sd} > 1.60 Å and R_{ch} > 2.55 Å were obtained.

The method underlying the ToposPro does not take into account the Coulomb interaction between the migrating cation and the ions of the host lattice. Such a drawback is eliminated in the bond valence sum (BVS) method.[24,25] Both VDP and BVS methods are relatively fast ways to study the mobility of a migrating cation in the structure, but they are not able to take into account the deformation of the lattice of the host structure that takes place during the migration of the cation through the saddle points. Sometimes this can be of large importance and leads to incorrect results.[21] This drawback is absent in the density functional theory nudged elastic band (DFT-NEB), and ab-initio molecular dynamics (AIMD) methods.

In this work, migration barriers for Ag^+ cation hops between adjacent interstitial sites were calculated using the nudged elastic band method as implemented in Quantum ESPRESSO.[26]

B. Results and Discussion

2.1. An analysis of migration topology by VDP approach.

The VDP approach provides a quick tentative insight into the Ag-ion migration. In particular, calculating the VDPs allows assessing the shape and size of the channel and cavity.[27] Figure S13a shows the representation of a channel in the crystal structure of $Ag_3B_6O_{10}I$, obtained by plotting of VDPs around Ag^+ cations. VDP polyhedra are formed by intersecting planes that bisect perpendicularly the lines joining atomic centers.[28] The parameter R_{SD} for VDP built around Ag^+ cation in an oxo-halide environment (coordination number *CN* = 6) is 1.71 Å. Herein, this value is reported for the first time, which was not reported by previous work.[27] Besides the atoms determining the VDP, there are additional atoms at a longer distance that can strongly influence the geometrical parameters of the VDP, in particular, its size and shape. To find these parameters ToposPro[19] constructs the VDP, taking into account all atoms in the structure. In contrast to the construction of polyhedra around Ag^+ cations only, the complex automated analysis of the entire structure revealed the presence of a continuous 3D net formed by the set of voids and channels (R_{sd} > 1.60 Å and R_{ch} > 2.55 Å) (Figure S13a). Thus, ionic conductivity can be achieved by hopping of Ag^+ cations between voids and it is worth noting that in addition to the two-dimensional ionic conductivity observed by us in the experiment, three-dimensional conductivity is possible (Figure S13a). However, voids that can connect two-dimensional channels into a three-dimensional network may not be available for ionic conductivity. Also for $Ag_3B_6O_{10}I$, the topology of the migration paths forms a bucket shape enveloping the iodine atom (Figure S13b).

2.2. A study of the effect of vacancy concentration on ionic conductivity by DFT-NEB method.

Despite some advantages of BVS over VDP, both methods still deal with a static model of the crystal structure, not considering possible lattice distortions or atoms displacements during the ion migration. These methods allow quick preliminary analysis and usually agree well with experimental data and the results obtained by more accurate methods such as molecular dynamics and density functional theory.[29,30] Nevertheless, in some cases there is a serious discrepancy in the data obtained by the methods of VDP and BVS and by much more sophisticated DFT-NEB method, as in the case of Li_2CoPO_4F.[21]

As the VDP analysis showed, for the $Ag_3B_6O_{10}I$ structure there are many voids into which silver cation can move (Figure S13). As the experimental XRD data showed (anharmonic probability density isosurfaces, Figure 5), with increasing temperature, Ag passes into these voids, in connection with which partially occupied positions appear, including those in the initial position of Ag2. In this case, according to these experimental data (XRD, Figure 5, and temperature dependence of the specific electrical conductivity, Figure 3b), the activation energy of ionic conduction decreases. Thus, it is expected that with the appearance of a partially occupied position in the Ag2 position and, accordingly, an increase in the concentration of vacancies in this position, a decrease in the activation energy is expected. To evaluate the influence of the vacancy concentration due to the appearance of partial occupancy with increasing temperature, we studied the DFT NEB migration by setting a vacancy at the Ag2 position (Figure S14a, snapshot no. 1). The Ag^+ migration energy barrier for $Ag_3B_6O_{10}I$ together with the optimized migration pathway optimized from the NEB method, are given in Figure S14. As it is shown, the migration pathway is a nearly straight line directed from the Ag2 site (Figure S14a, snapshot no. 1) to the vacancy site in the Ag2 site (Figure S14a, snapshot no. 9). The maximum energy occurs when Ag^+ passes through the rectangular face (Figure S14a, snapshot no. 5). In this case, Ag^+ becomes coordinated by four oxygen ions. It should also be noted that the voids corresponding to snapshots no. 1-3 and 5-9 can be easily accessed by Ag^+, even at low temperatures. This observation is in agreement with the results obtained by anharmonic probability density isosurfaces obtained from XRD data (Figure 5): at 25 °C the Ag^+ cations become smeared in the direction of the migration pathway proposed. The diffusion energy barrier for $Ag_3B_6O_{10}I$ structure 1 with a vacancy being created in the Ag2 site is 0.21 eV, which is much lower than the case when both positions of Ag2 are completely occupied (0.72 eV, Figure 5, 25 °C). Thus, using the DFT NEB method, we have shown that the presence of a vacancy has a significant effect on lowering the activation energy. In our experiment, vacancies were created by heating and jumping some of the silver atoms in the positions of voids that we found experimentally and by the VDP method. However, vacancies in the silver sublattice can be created chemically upon synthesis by varying the composition of the material (by doping and creating an excess of the positive charge of the framework).

C. Supplementary Figures

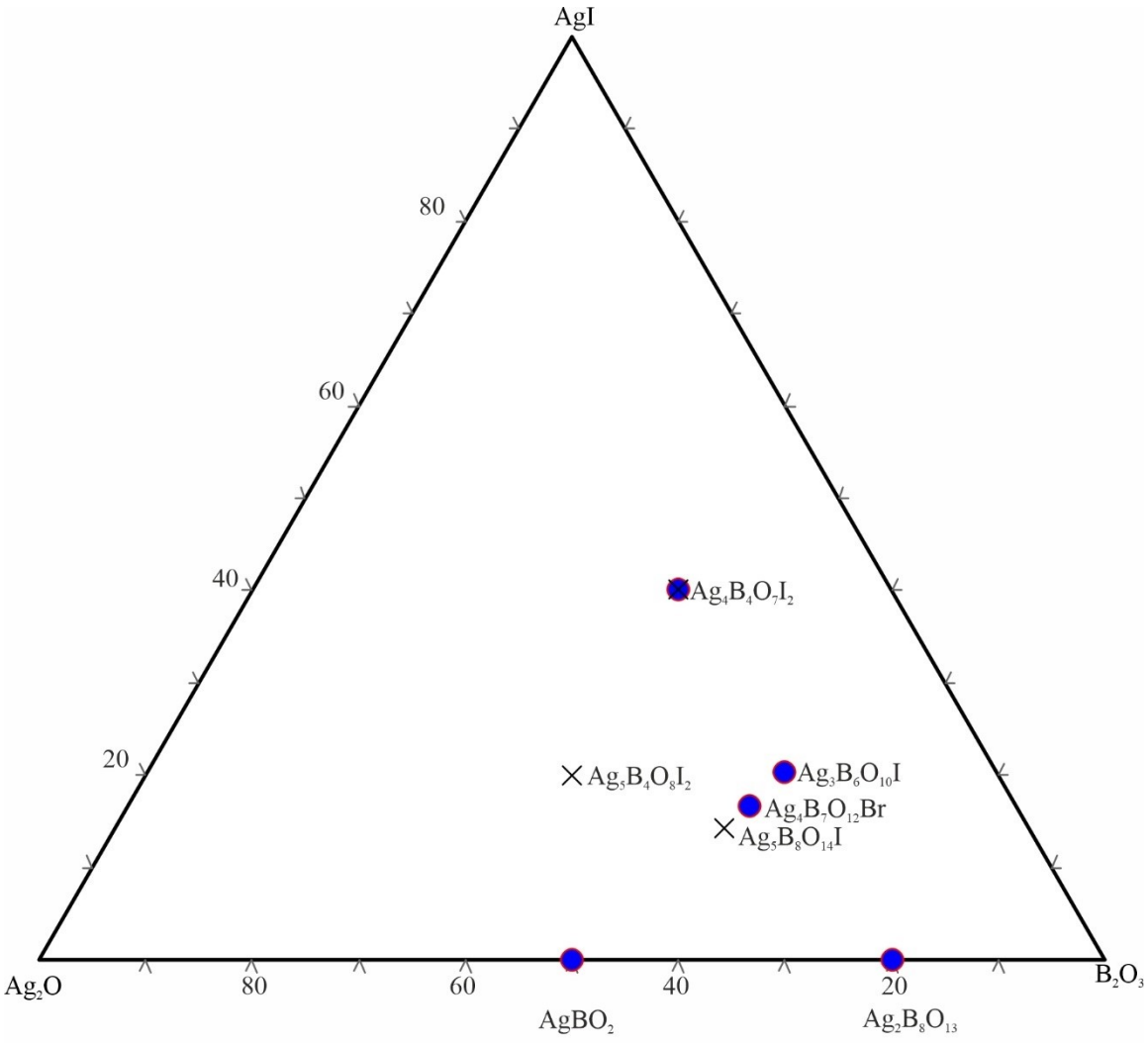

Figure S1. The figurative points on the Ag_2O−AgI−B_2O_3 phase diagram. The crosses show the data from [31] while the blue points show the compounds with studied crystal structures.

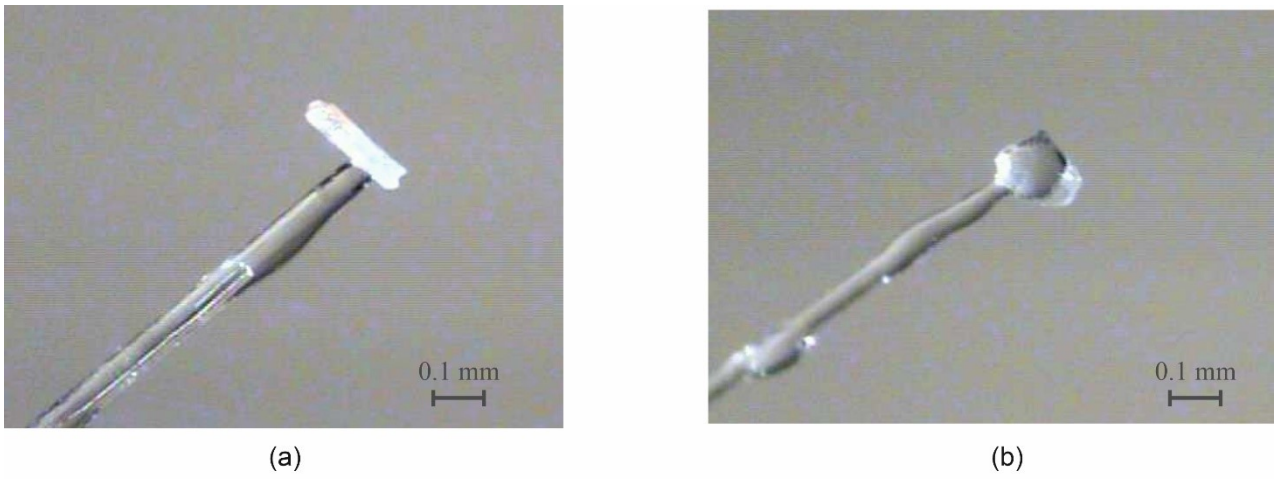

(a) (b)

Figure S2. Single crystals of (a) $Ag_3B_6O_{10}I$ and (b) $Na_3B_6O_{10}I$.

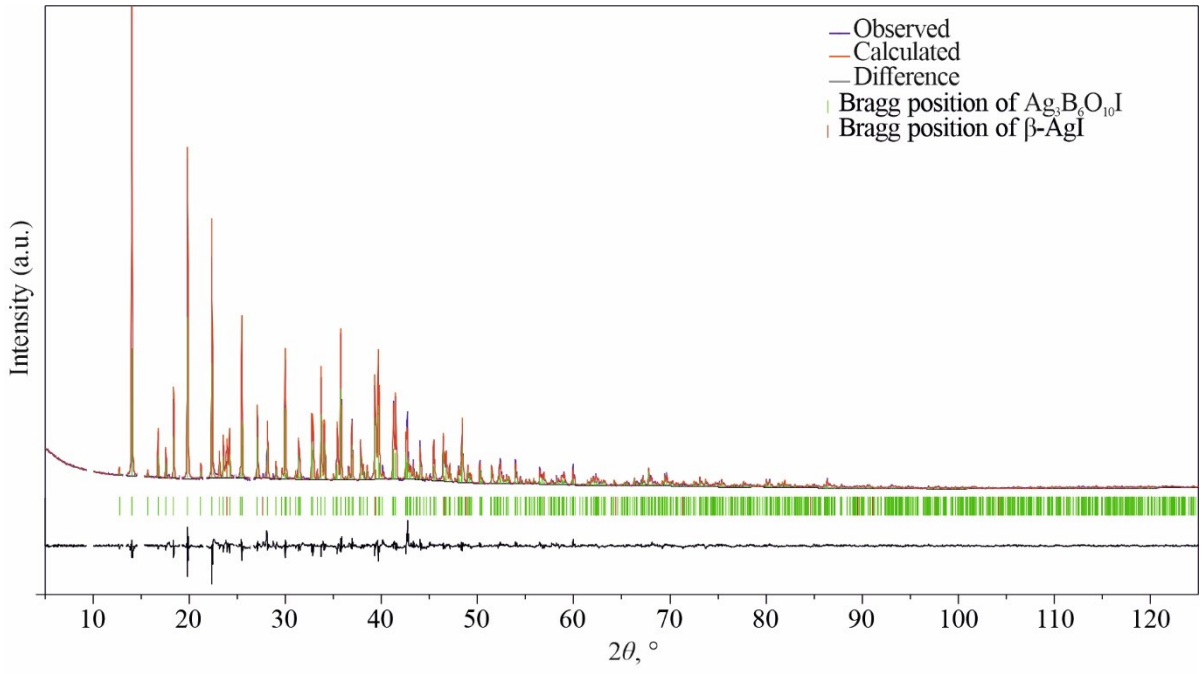

Figure S3. Intensity profiles for the powder X-ray Rietveld refinement of $Ag_3B_6O_{10}I$. The observed and calculated profiles are represented in blue and red lines, respectively. The difference profile is plotted at the bottom. Vertical bars indicate the positions of the Bragg reflections. The minor impurity peaks at 9.68, 14.71 and 26.55 ° 2θ were excluded from the Rietveld refinement..

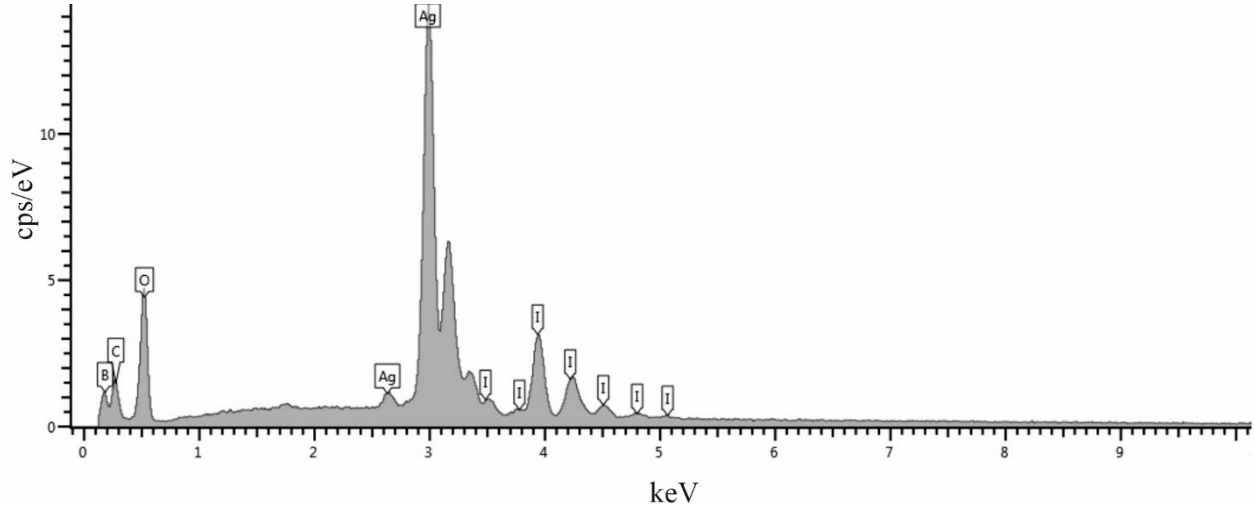

Figure S4. EDX spectrum of $Ag_3B_6O_{10}I$.

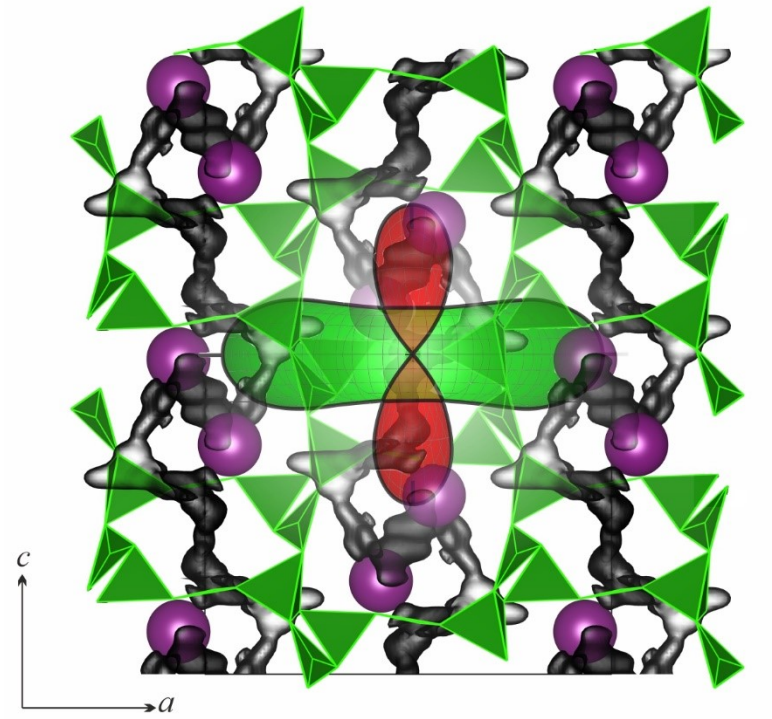

Figure S4. Crystal structure of *α*-$Ag_3B_6O_{10}I$ viewed along [010] versus thermal expansion tensor at 200 °C. For silver cations, the joint probability density function (JPDF) (grey) shows the migration paths.

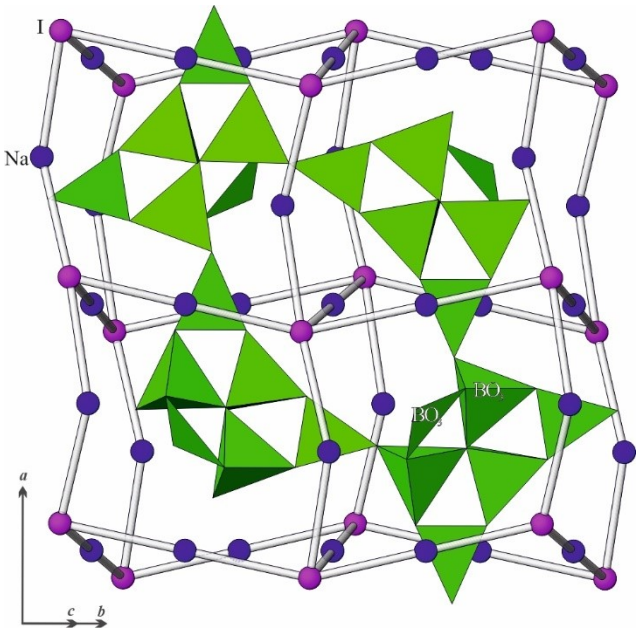

Figure S5. Crystal structure of $Na_3B_6O_{10}I$.

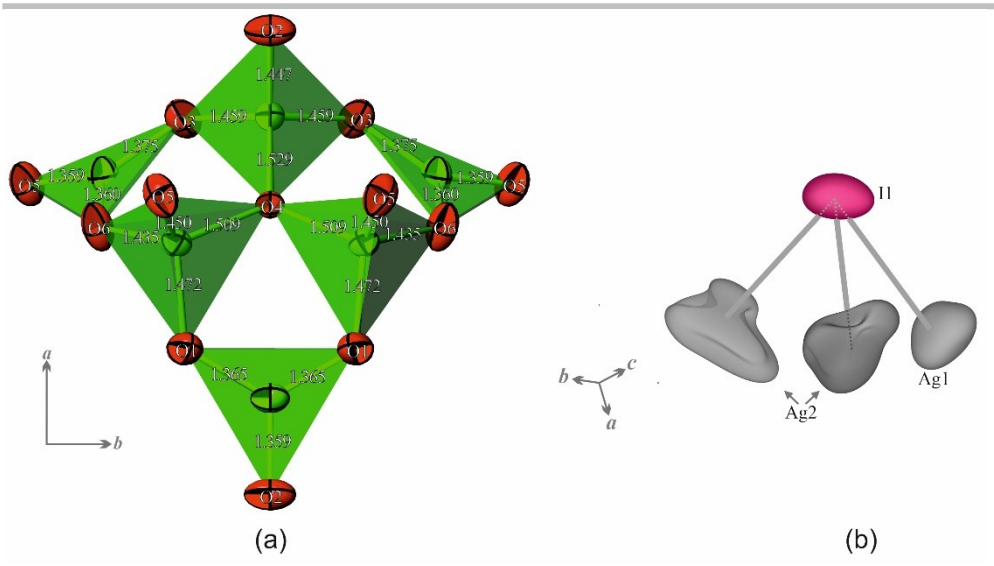

Figure S6. (a) The B_6O_{13} and (b) IAg_3 groups in the structure of $Ag_3B_6O_{10}I$.

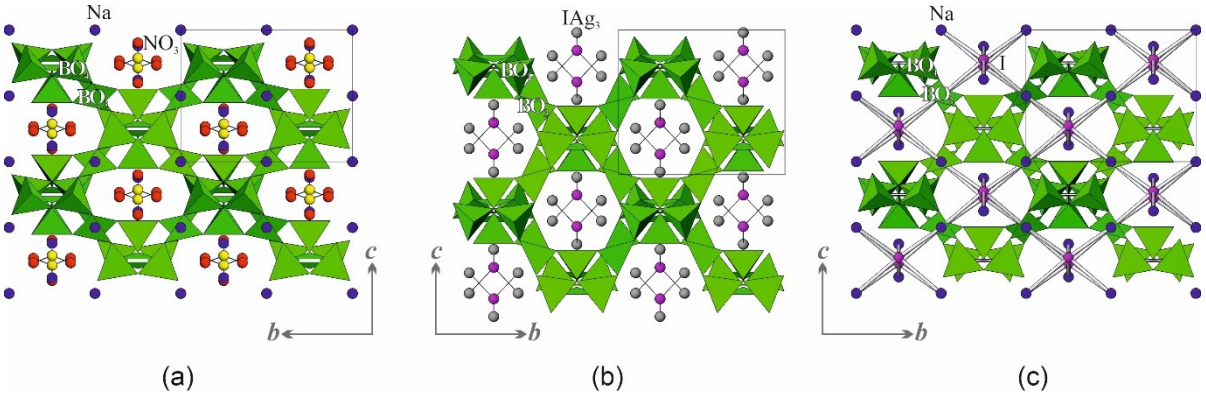

Figure S7. Crystal structures of (a) $Na_3B_6O_{10}(NO_3)$, (b) $Ag_3B_6O_{10}I$ and (c) $Na_3B_6O_{10}I$.

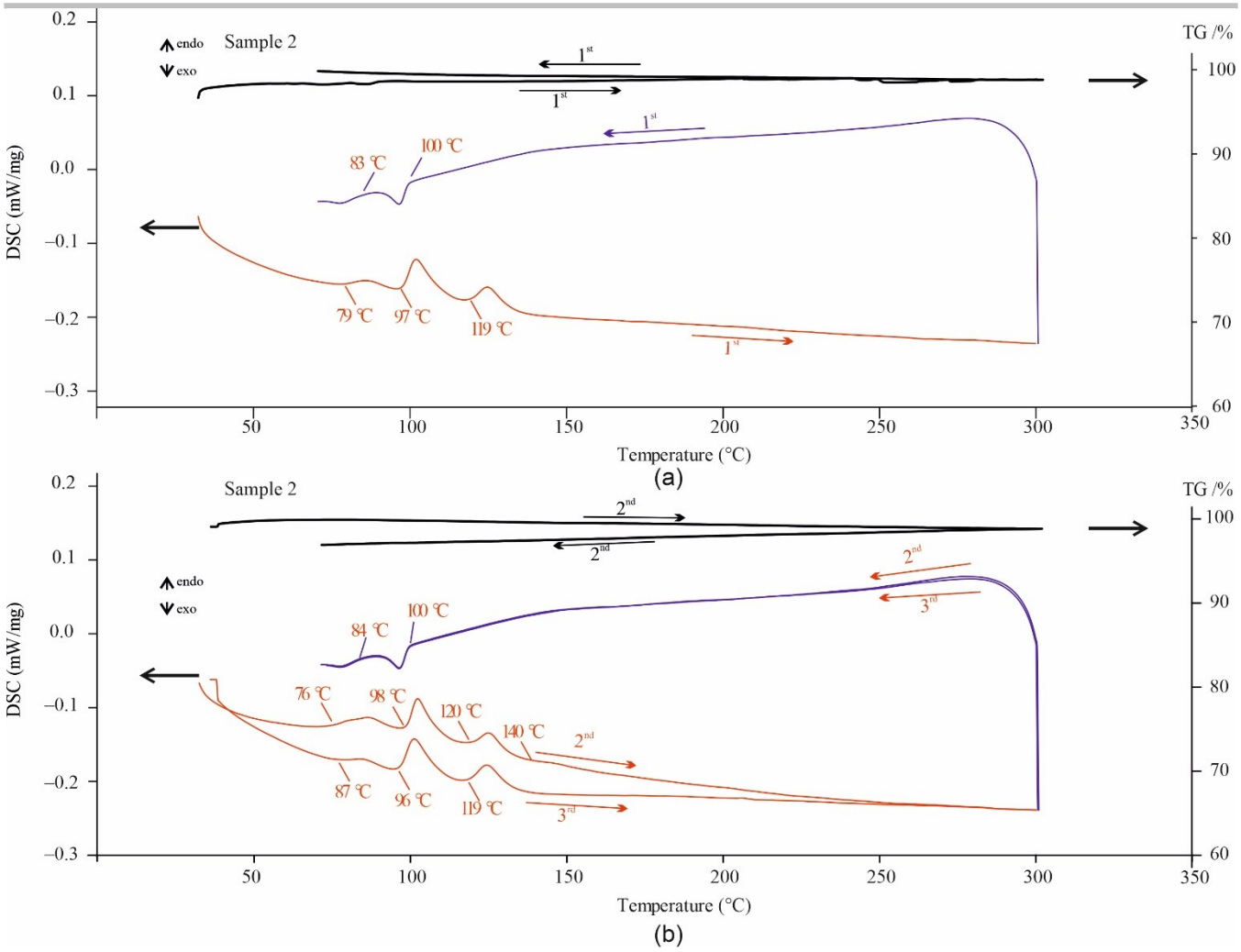

Figure S8. TG and DSC curves of $Ag_3B_6O_{10}I$. (a) 1st and (b) 2nd and 3rd heating/cooling cycles. The curve corresponding to the third cycle is not shown as it coincides with that for the second one. The thermal effect at 140 °C corresponds to the β↔α transition of the AgI impurity (2 wt %). Using the known enthalpy of this transition (26.9 J/g)[32], one can estimate the expected thermal effect as ~0.5 J/g which is close to the observed value of ~0.3 J/g at 140 °C.

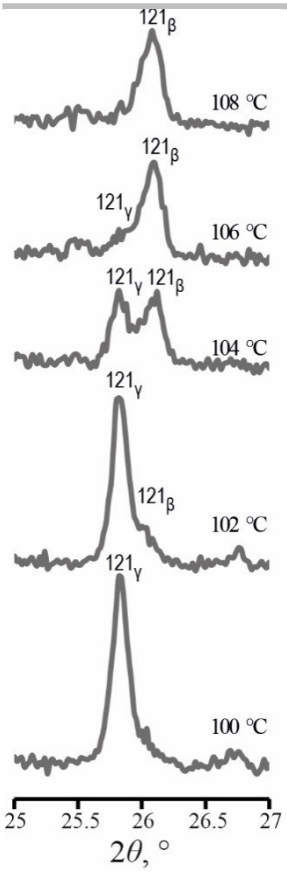

Figure S8. The diffraction pattern around the position of the (121) reflection at various temperatures.

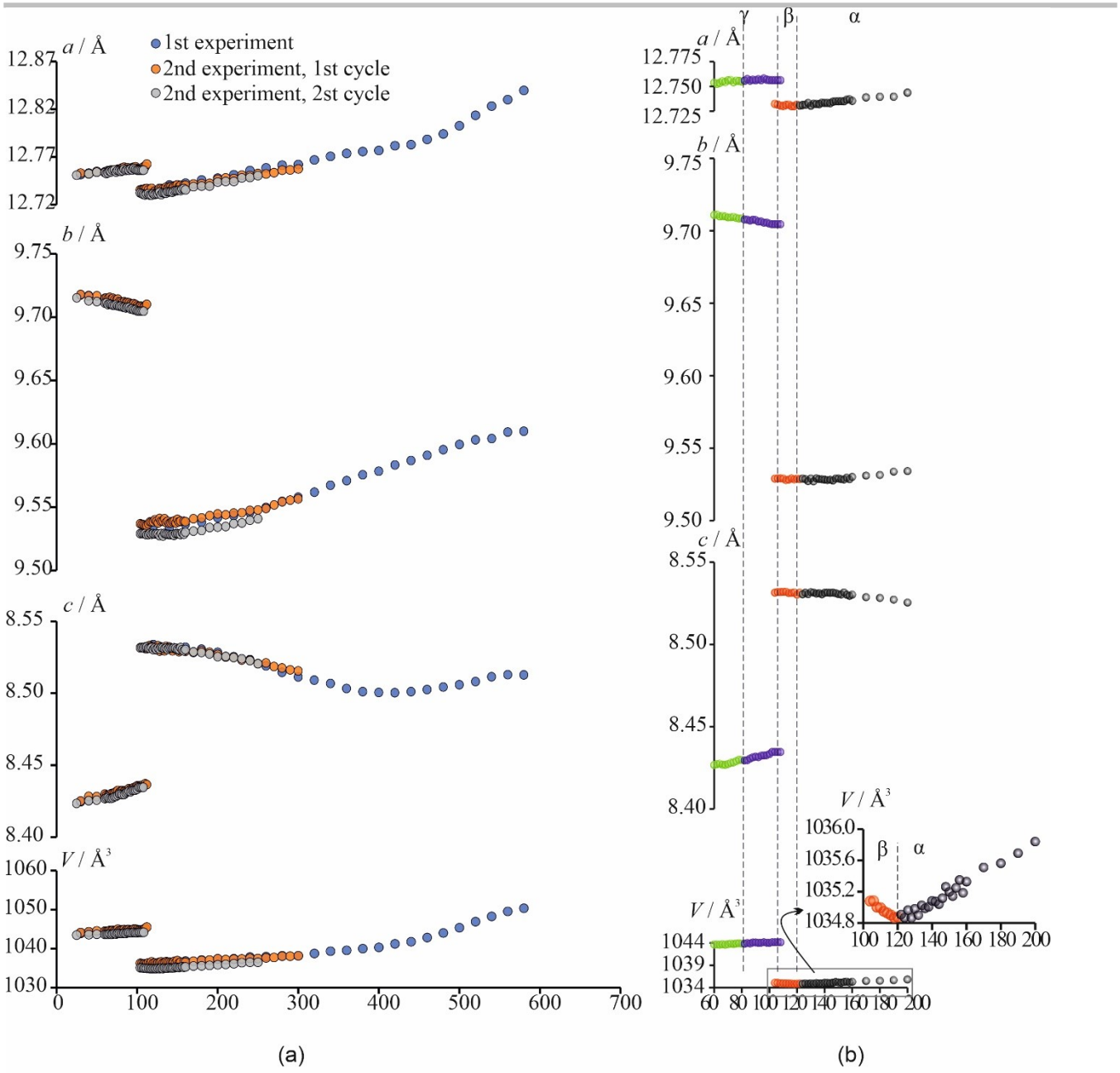

Figure S10. Temperature dependences of the unit-cell parameters and volume for $Ag_3B_6O_{10}I$. (*a*) Full temperature range; (*b*) Detailed view on the 60−100 °C temperature range for second experiment, second cycle. Uncertainties of unit cell parameters and volume are smaller than the used symbols. Blue points in (b): *δ*-$Ag_3B_6O_{10}I$; green points in (b): *γ*-$Ag_3B_6O_{10}I$; red points in (b): *β*-$Ag_3B_6O_{10}I$; dark points in (b): *α*-$Ag_3B_6O_{10}I$.

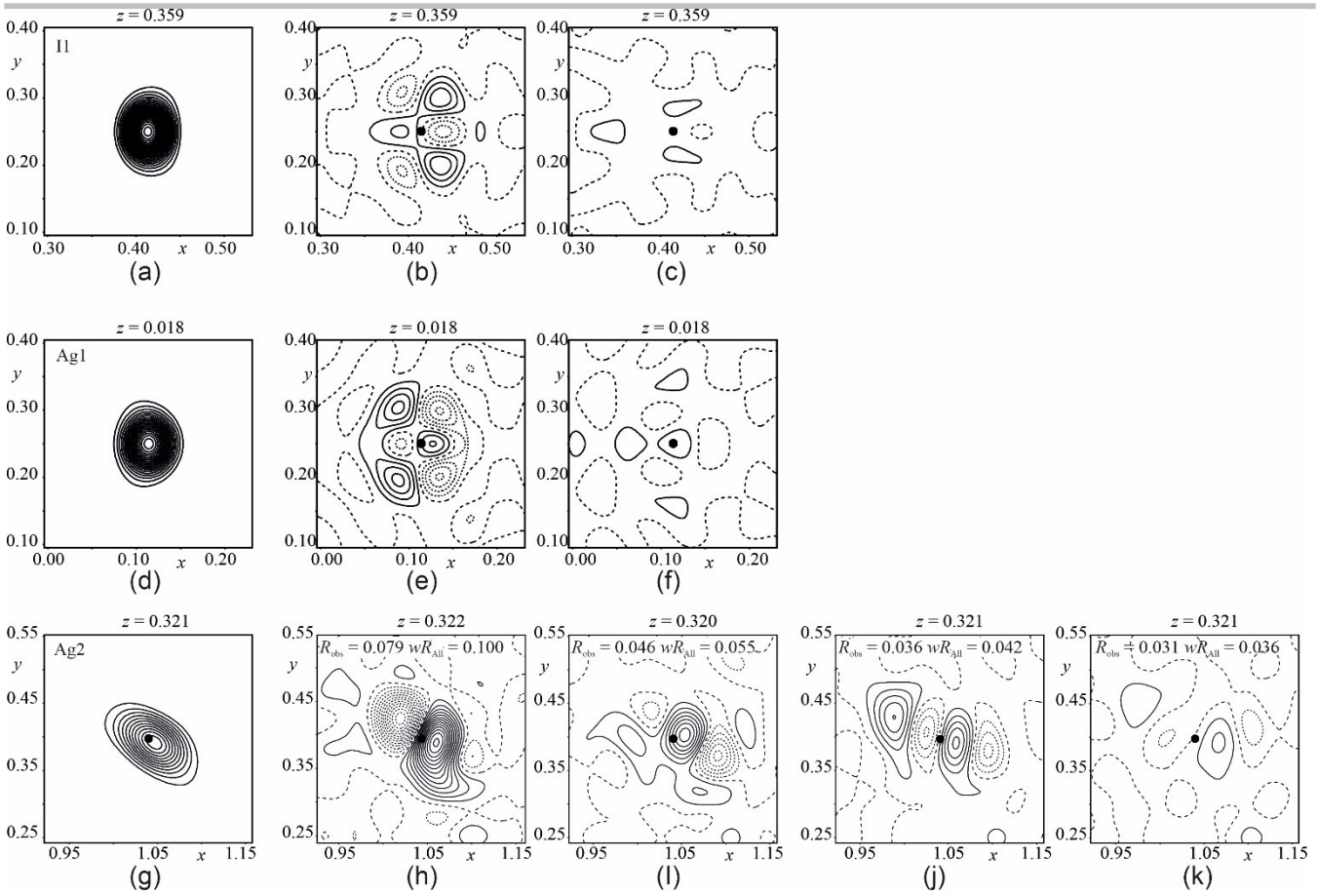

Figure S11. Fourier map of the electron-density distribution for $Ag_3B_6O_{10}I$ centered on iodine and silver atoms. *Upper row*: (a) observed Fourier maps, difference Fourier maps for (b) anisotropic, and (c) anharmonic third-order model refinement for I1 atom. *Next row*: (*d*) observed Fourier maps, difference Fourier maps for (*e*) anisotropic, and (*f*) anharmonic third-order model refinement for Ag1 atom. *Bottom row*: (*g*) observed Fourier maps, difference Fourier maps for (*h*) anisotropic, and anharmonic (*l*) third-order, (j) fourth-order and (k) fifth-order model refinement for Ag2 atom. Contour lines are in intervals of 10 e × Å^{-3} for observed maps and 0.5 e × Å^{-3} for the difference ones. The positive electron density values are shown in continuous lines while the negative values are shown in dashed lines.

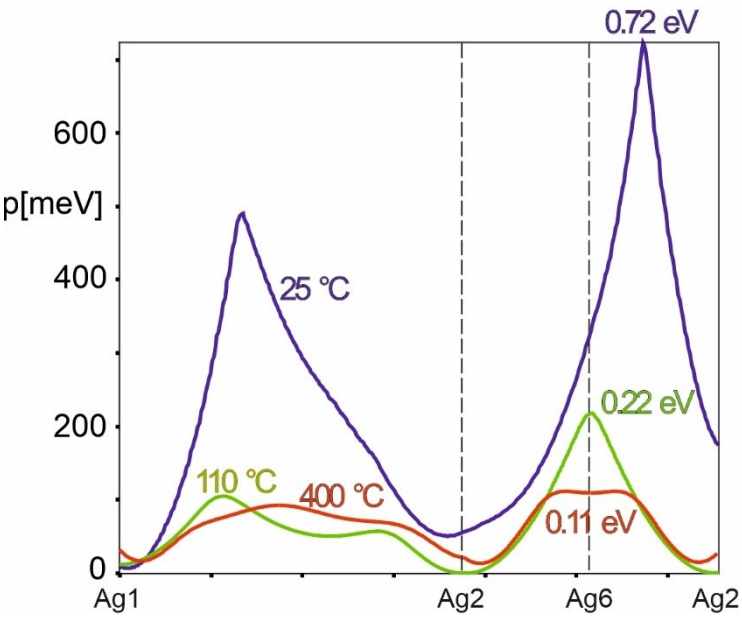

Figure S12. One-particle potential along Ag1–Ag2–Ag2 (at 25 and 110 °C) and Ag1–Ag2–Ag6–Ag2 (at 400 °C) diffusion path in the structure of $Ag_3B_6O_{10}I$.

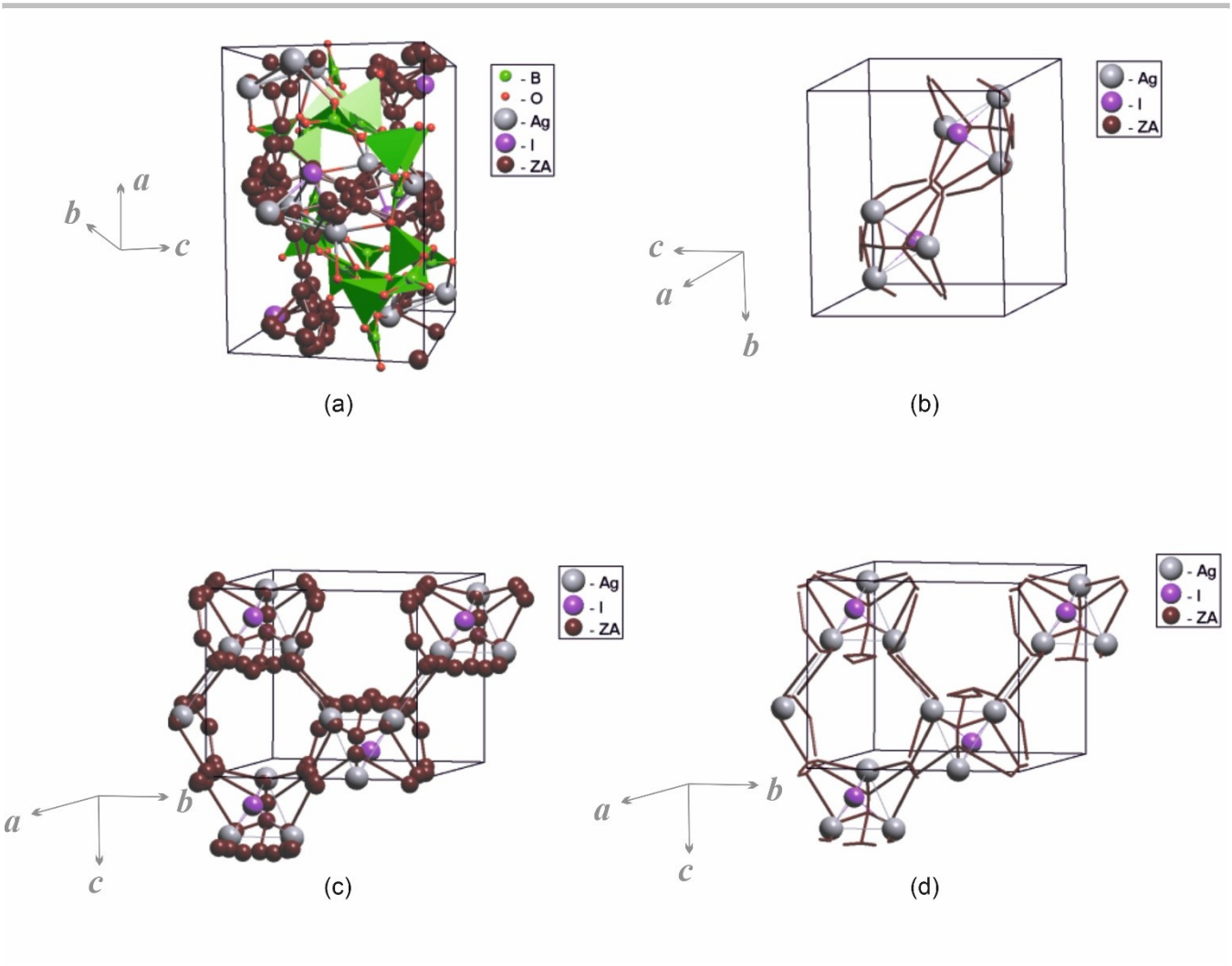

Figure S13. (a,c,d) The VDP produced system of voids and channels (black spheres and sticks, ZA) in the structure of $Ag_3B_6O_{10}I$. The topology of the migration paths forms a bucket shape enveloping the iodine atom (b).

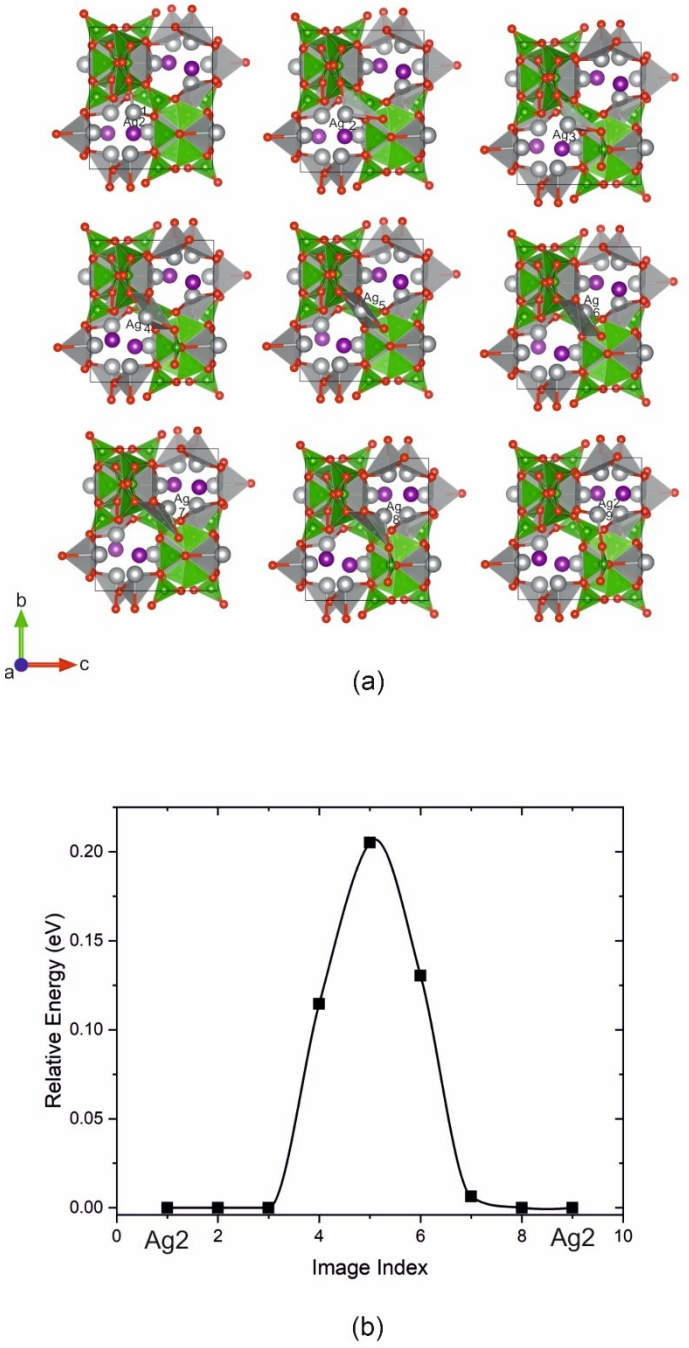

Figure S14. (a) NEB snapshots for the Ag^+ cation migrating along the Ag2−Ag2 diffusion path in the structure of $Ag_3B_6O_{10}I$ with one Ag vacancy per cell. Boron atoms are in green, while red, grey, and violet represent O, Ag and I atoms, respectively. Reconnected bonds show of migrating Ag atom how the atom environment is rearranged for crystal upon the migration along the Ag2−Ag2 direction. (b) The corresponding diffusion energy barrier.

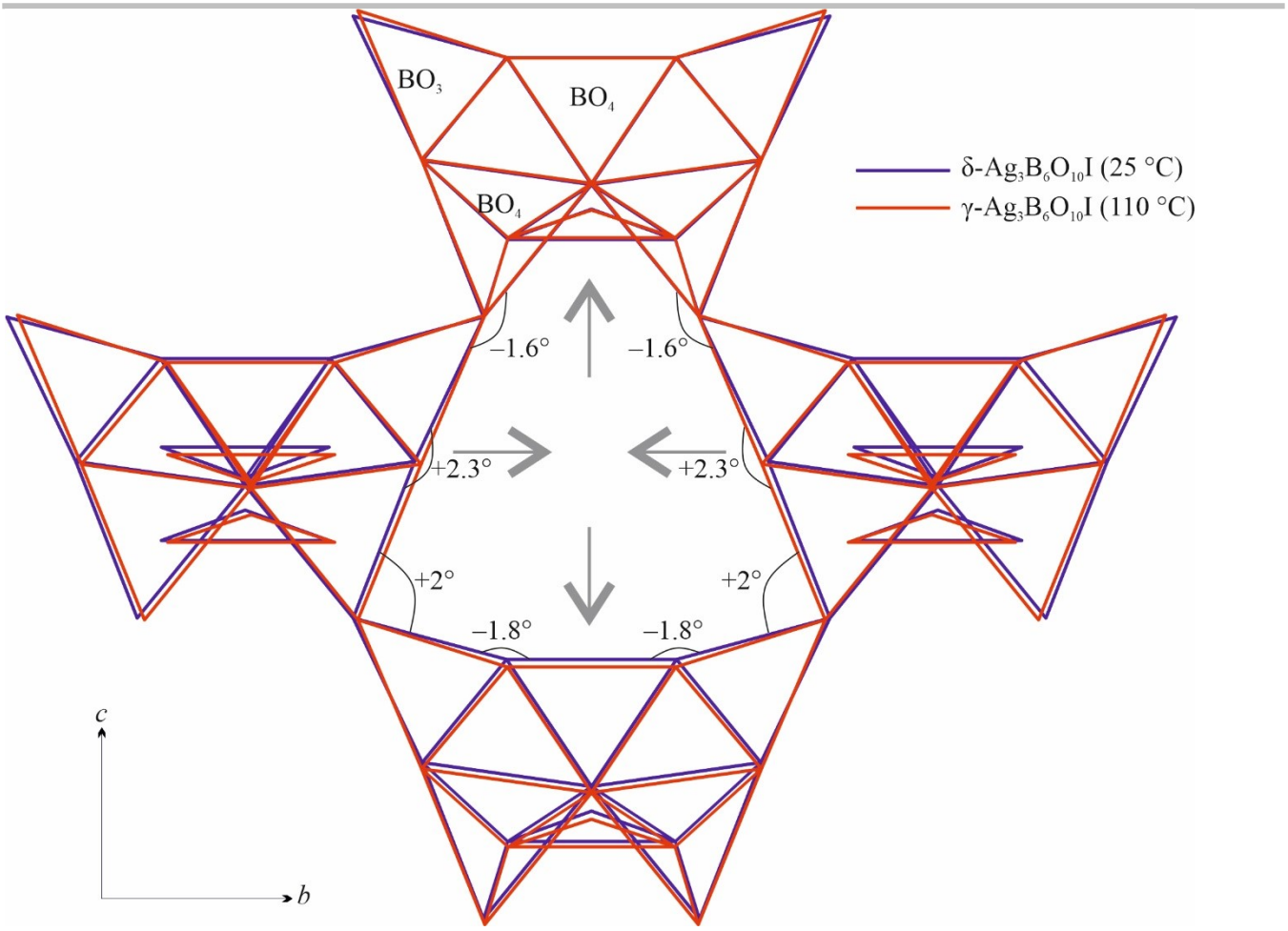

Figure S15. Changing of O–O–O angles during δ↔γ↔β phase transition in structure $Ag_3B_6O_{10}I$.

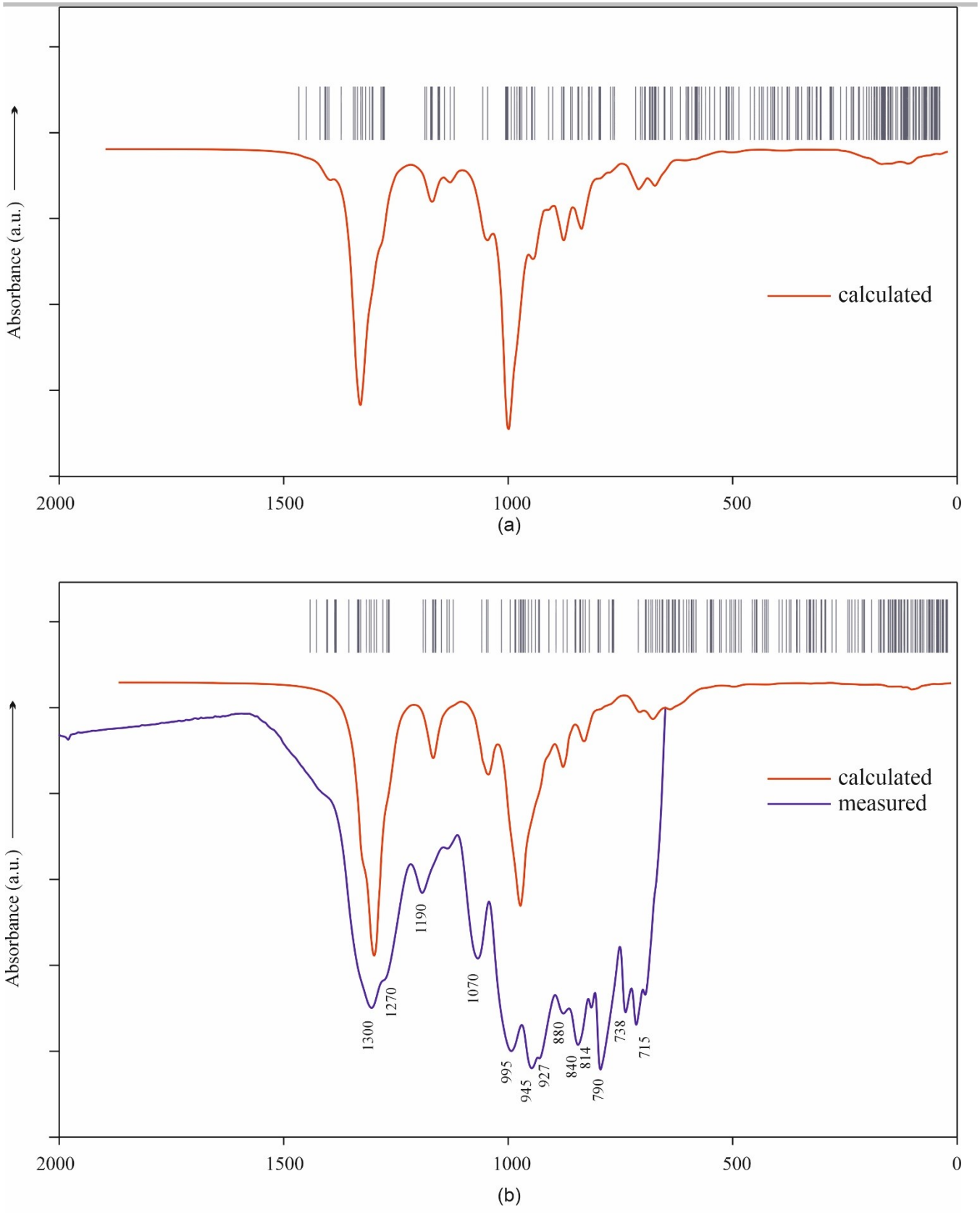

Figure S16. (a) The calculated IR spectrum of $Na_3B_6O_{10}I$ and (b) measured and calculated IR spectra of $Ag_3B_6O_{10}I$.

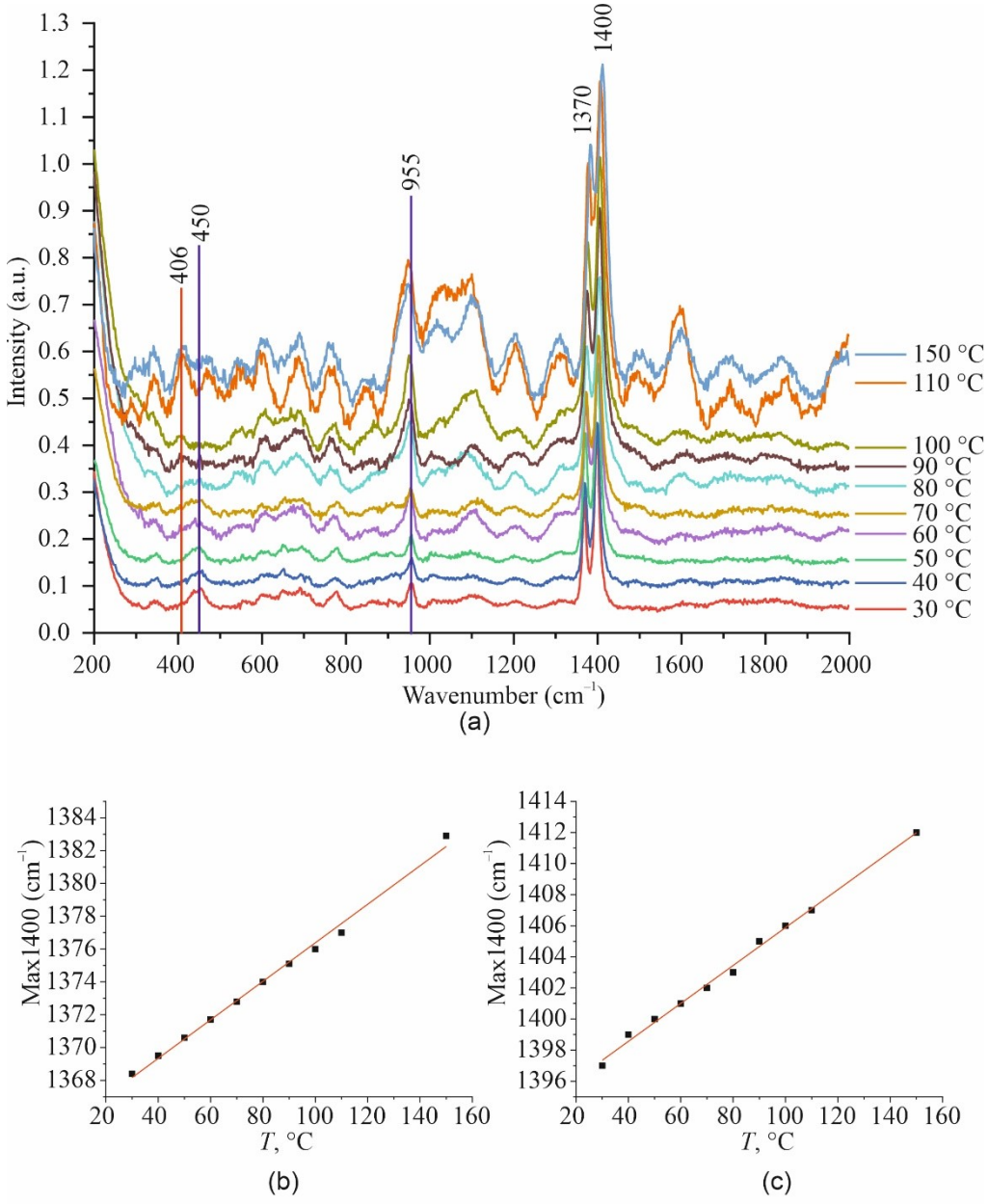

Figure S17. Raman spectra of $Ag_3B_6O_{10}I$ at (a) different temperatures and thermal dependences of (b) 1370 cm^{-1} and (c) 1400 cm^{-1} bands.

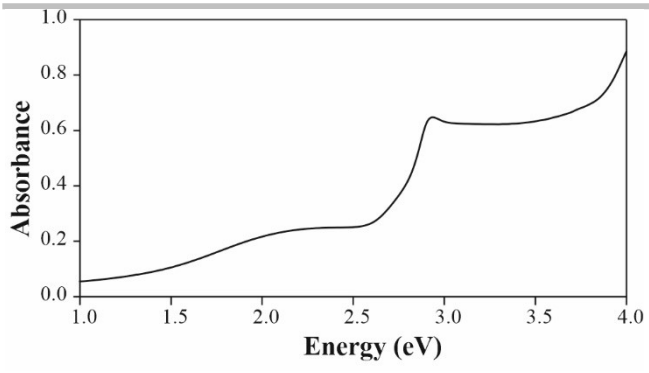

Figure S18. Absorption spectrum of $Ag_3B_6O_{10}I$.

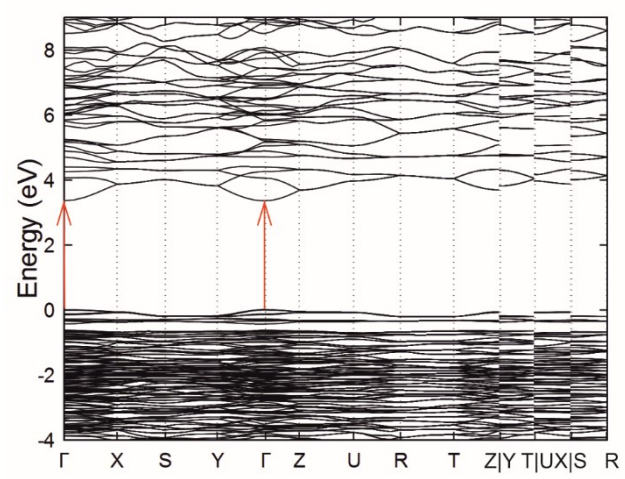

Figure S19. The band structure of $Ag_3B_6O_{10}I$ (the Fermi level is set at 0 eV).

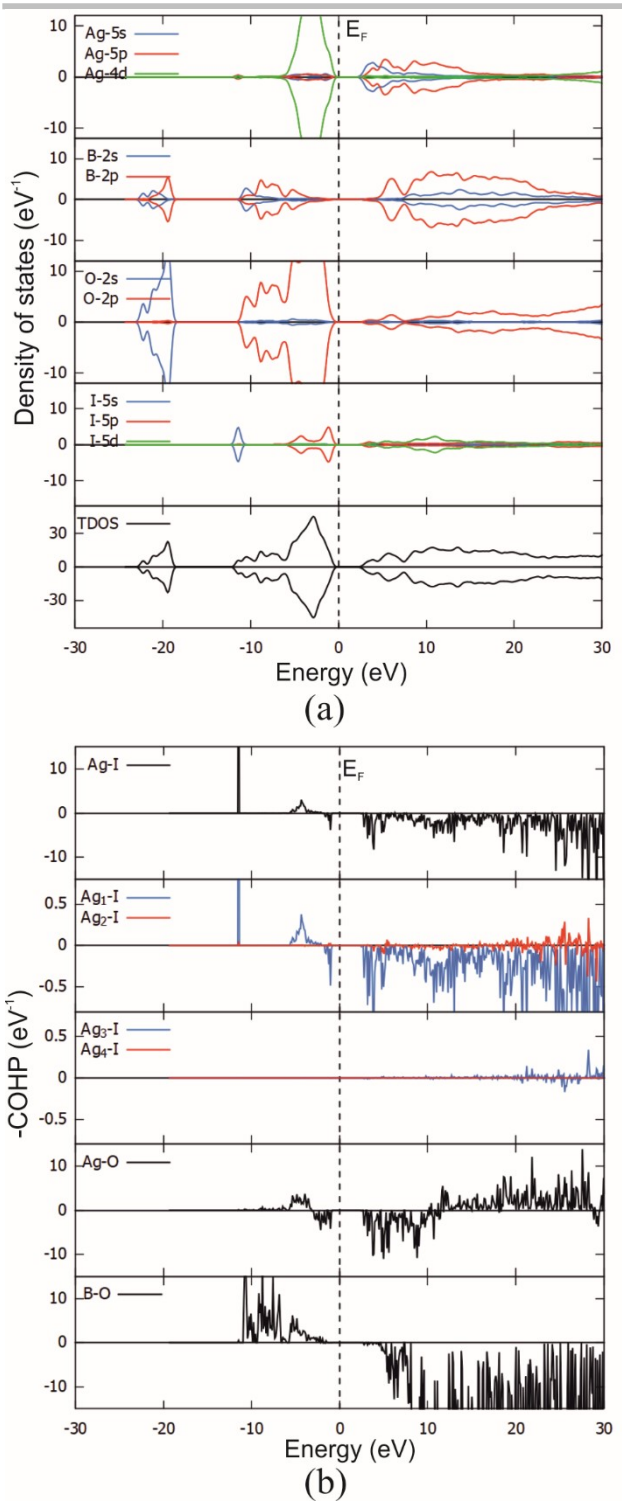

Figure S20. The total and partial density of states (a) and Crystal Orbital Hamilton Population (COHP) of $Ag_3B_6O_{10}I$ plotted using the same scale on the abscissa axis. Following convention, we multiplied the COHP values by – so that bonding (anti-bonding) interactions are positive (negative). Ag atoms in the nearest environment of I are indicated by indices (see Fig. 3). For all graphs: The Fermi level has been offset to 0 eV.

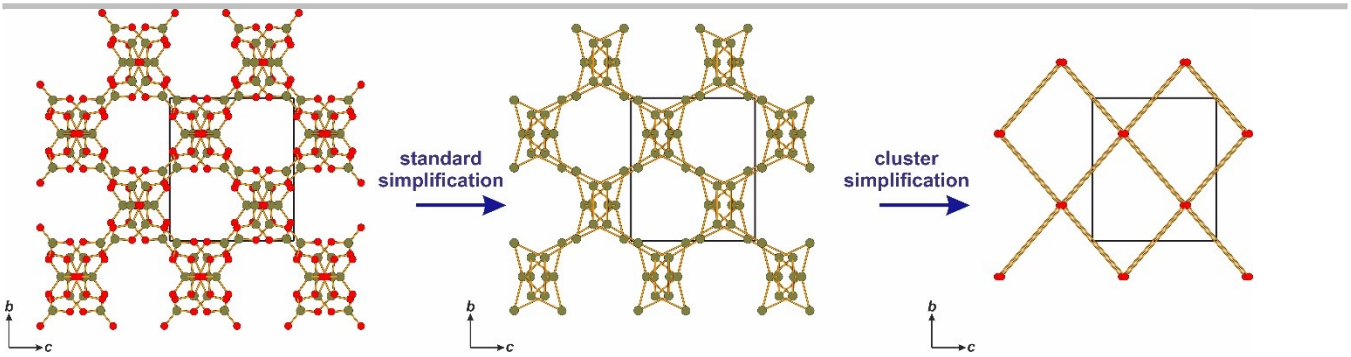

Figure S21. Topology of the heteropolyhedral $[B_6O_{10}]$-framework of the centrosymmetric compounds in the $M_3B_6O_{10}X$ family including $M_3B_6O_{10}I$, M= Ag, Na (s.g. *Pmna*) as well as $Na_3B_6O_{10}Cl$ and $Na_2RbB_6O_{10}Cl$ (s.g. $P2_12_12_1$).

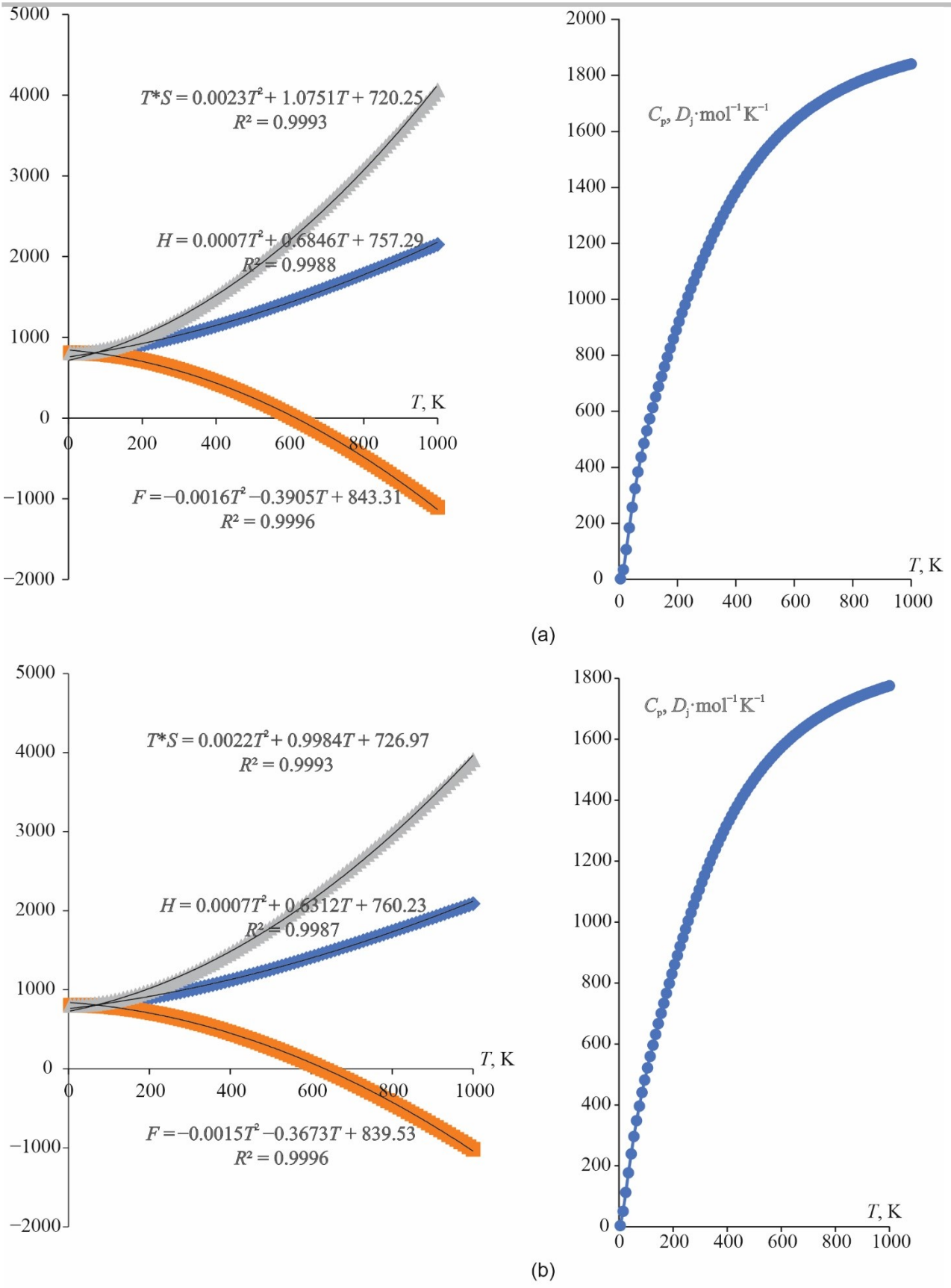

Figure S22. Enthalpy, free energy, entropy in [kDj/mol] and isobaric heat capacity of (a) $Na_3B_6O_{10}I$ and (b) $Ag_3B_6O_{10}I$ as a functions of temperature.

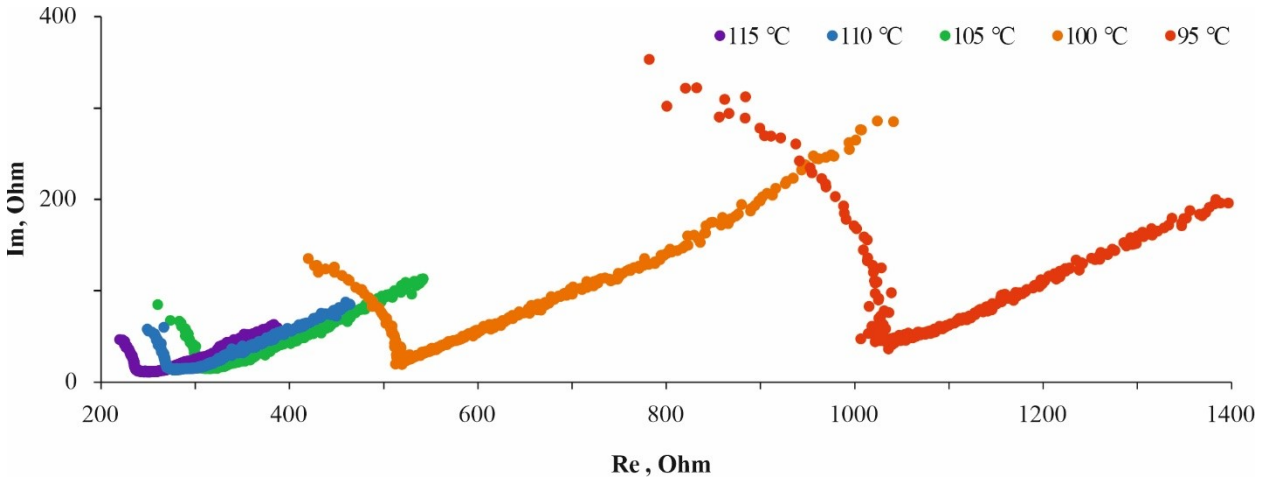

Figure S23. Complex impedance of a the $Ag_3B_6O_{10}I$ at different temperatures.

D. Supplementary Tables

Table S1. Experimental details for $M_3B_6O_{10}I$, M = Na, Ag

	$Na_3B_6O_{10}I$	δ-$Ag_3B_6O_{10}I$
CCDC number	2154417	2154414
Crystal data		
Chemical formula	$Na_3B_6O_{10}I$	$Ag_3B_6O_{10}I$
Temperature (°C)	25	25
Crystal data		
M_r	210.4	337.7
Crystal system, space group	Orthorhombic, *Pnma*	
a, *b*, *c* (Å)	12.8162 (6), 9.9063 (5), 7.6762 (4)	12.7566 (15), 9.7050 (12), 8.4295 (10)
V (Å^3)	974.58 (8)	1043.6 (2)
Z	4	
Radiation type	Mo *K*α	
μ (mm^{-1})	3.47	8.58
Crystal size (mm)	0.107×0.162×0.175	0.084×0.122×0.276
Data collection		
Diffractometer	Bruker Smart APEX II	
Absorption correction	Analytical[32]	
No. of measured, independent and observed [$I > 3\sigma(I)$] reflections	16847, 2312, 1821	17792, 2460, 1842
R_{int}	0.045	0.039
(sin θ/λ)$_{max}$ (Å^{-1})	0.822	0.822
Refinement		
$R[F^2 > 2\sigma(F^2)]$, $wR(F^2)$, S	0.028, 0.031, 1.33	0.031, 0.038, 1.66
No. of reflections	2312	2460
No. of parameters	104	131
$\Delta\rho_{max}$, $\Delta\rho_{min}$ (e Å^{-3})	1.70, −0.96	1.72, −1.41

Table S2. Experimental details for variable temperatures single-crystal X-ray diffraction studies of $Ag_3B_6O_{10}I$

	β-$Ag_3B_6O_{10}I$	α-$Ag_3B_6O_{10}I$	α-$Ag_3B_6O_{10}I$	α-$Ag_3B_6O_{10}I$	α-$Ag_3B_6O_{10}I$
CCDC number	2154415	2154413	2154411	2154416	2154412
Crystal data					
Chemical formula	$Ag_3B_6O_{10}I$	$Ag_3B_6O_{10}I$	$Ag_3B_6O_{10}I$	$Ag_3B_6O_{10}I$	$Ag_3B_6O_{10}I$
M_r	675.4	675.4	675.4	675.4	675.4
Crystal system, space group	Orthorhombic, *Pnma*	Orthorhombic, *Pnma*	Orthorhombic, *Pnma*	Orthorhombic, *Pnma*	Orthorhombic, *Pnma*
Temperature (°C)	110	120	140	300	400
a (Å),	12.7504 (5),	12.7477 (5),	12.7428 (6),	12.7702 (6),	12.7726 (7),
b (Å),	9.5370 (3),	9.5347 (3),	9.5341 (3),	9.5617 (4),	9.5739 (5),
c (Å)	8.5317 (3)	8.5287 (3)	8.5326 (3)	8.5156 (4)	8.4899 (5)
V (Å^3)	1037.46 (6)	1036.63 (6)	1036.64 (7)	1039.80 (8)	1038.18 (10)
Z	4	4	4	4	4
Radiation type	Mo *K*α	Mo *K*α	Mo *K*α	Mo *K*α	Mo *K*α
μ (mm^{-1})	8.63	8.63	8.63	8.61	8.62
Crystal size (mm)	0.16 × 0.13 × 0.06				
Data collection					
Diffractometer	XtaLAB Synergy, Single source at home/near, HyPix				
Absorption correction	Multi−scan, *CrysAlis PRO* 1.171.41.104a (Rigaku Oxford Diffraction, 2021) Empirical absorption correction using spherical harmonics, implemented in SCALE3 ABSPACK scaling algorithm.[3]				
T_{min}, T_{max}	0.431, 0.724	0.431, 0.726	0.431, 0.727	0.416, 0.728	0.414, 0.733
No. of measured, independent and observed [$I > 3\sigma(I)$] reflections	4815, 1300, 961	4830, 1296, 960	4881, 1296, 969	4860, 1283, 712	4714, 1271, 761
R_{int}	0.044	0.047	0.053	0.052	0.059
(sin θ/λ)$_{max}$ (Å^{-1})	0.686	0.686	0.685	0.684	0.688
Refinement					
$R[F^2 > 2\sigma(F^2)]$, $wR(F^2)$, S	0.060, 0.073, 3.16	0.060, 0.076, 3.21	0.059, 0.076, 3.24	0.058, 0.063, 2.39	0.060, 0.068, 2.37
No. of reflections	1300	1296	1296	1283	1271
No. of parameters	163	151	159	203	178
$\Delta\rho_{max}$, $\Delta\rho_{min}$ (e Å^{-3})	1.65, −1.42	1.78, −1.52	1.50, −1.13	1.15, −1.13	1.07, −0.94

Computer programs: *CrysAlis PRO* 1.171.41.104a (Rigaku OD, 2021)[3].

Table S3. The order of anharmonic terms used in description of the silver vibrations in the structure of $Ag_3B_6O_{10}I$.

Atom	25 °C	110 °C	120 °C	140 °C	300 °C	400 °C
I1	3	4	3	4	4	4
Ag1	3	4	3	4	4	4
Ag2	5	4	4	4	4	4
Ag3	–	3	3	3	4	4
Ag4	–	3	anisotropic	anisotropic	4	3
Ag5	–	anisotropic	anisotropic	anisotropic	3	4
Ag6	–	–	–	–	–	anisotropic

Table S4. The list of fixed to zero anharmonic parameters for $Ag_3B_6O_{10}I$ at different temperatures

	third-order	fourth-order	fifth-order
		25 °C	
I1	$C_{111}, C_{113}, C_{133}, C_{333}$		
Ag1	C_{111}		
Ag2	$C_{111}, C_{112}, C_{113}, C_{333},$	$D_{1111}, D_{1112}, D_{1113},$	$E_{11113}, E_{11123}, E_{11133}, E_{11223}, E_{11223}, E_{11233}, E_{11333}, E_{12223}, E_{12233}, E_{12333}, E_{13333}, E_{22223}, E_{22233}, E_{22333}, E_{23333}, E_{33333}$
		110 °C	
I1	C_{113}	D_{1111}, D_{1122}, D_{1223}, D_{1333}, D_{2222}, D_{3333}	
Ag1	C_{111}	$D_{1111}, D_{1113}, D_{1223}, D_{1333}, D_{2233}, D_{3333}, D_{1133}$	
Ag2	$C_{111}, C_{122}, C_{223}, C_{133}, C_{222}\, C_{233}$	$D_{1122}, D_{1123}, D_{1133}, D_{2233}, D_{1111}, D_{1112}, D_{1113}, D_{1222}, D_{1223}, D_{1233}, D_{1333}, D_{2222}, D_{2223}, D_{2333}$	
Ag3	C_{223}	-	
Ag4	$C_{113}, C_{133}, C_{222}$	-	
		120 °C	
I1	C_{113}		
Ag1	C_{111}		
Ag2	$C_{111}, C_{122}, C_{223}, C_{233}, C_{223}$	$D_{1111}, D_{1112}, D_{1113}, D_{1122}, D_{1123}, D_{1133}, D_{1222}, D_{1223}, D_{1233}, D_{2222}, D_{2223}, D_{2233}, D_{2333}, D_{1333}$	
		140 °C	
I1	C_{113}	$D_{1223}, D_{1333}, D_{2222}, D_{3333}$	
Ag1	C_{111}	$D_{1111}, D_{1223}, D_{1333}, D_{3333}, D_{1113}$	
Ag2	$C_{222}, C_{122}, C_{223}, C_{233}, C_{223}$	$D_{1111}, D_{1112}, D_{1113}, D_{1122}, D_{1123}, D_{1133}, D_{1222}, D_{1223}, D_{1233}, D_{1333}, D_{2222}, D_{2223}, D_{2233}, D_{2333}$	
		300 °C	
I1	-	$D_{1111}, D_{1113}, D_{1223}, D_{1333}, D_{2222}, D_{3333}$	
Ag2	C_{112}, C_{122}		
Ag3	C_{133}, C_{223}		
Ag5	$C_{111}, C_{113}, C_{123}, C_{223}, C_{333}$		
		400 °C	
I1		$D_{1111}, D_{1113}, D_{1223}, D_{1333}, D_{2222}, D_{3333}$	
Ag1	C_{111}	$D_{1111}, D_{1113}, D_{1133}, D_{1223}, D_{1333}, D_{2233}, D_{1122}, D_{3333}$	
Ag2	$C_{111}, C_{112}, C_{122}, C_{133}, C_{222}, C_{223}$	$D_{1111}, D_{1112}, D_{1122}, D_{1133}, D_{1222}, D_{1223}, D_{1233}, D_{1333}, D_{2222}, D_{2223}, D_{2233}, D_{2333}, D_{1123}, D_{1113}$	
Ag3	$C_{133}, C_{223}, C_{122}$	$D_{1122}, D_{1223}, D_{2222}, D_{2233}$	
Ag4	$C_{111}, C_{112}, C_{113}, C_{122}, C_{123}, C_{133}, C_{223}, C_{333}, C_{222}$	$D_{1113}, D_{1122}, D_{1123}, D_{1133}, D_{1222}, D_{1223}, D_{1233}, D_{1333}, D_{2222}, D_{2223}, D_{2233}, D_{2333}, D_{3333}$	
Ag5	$C_{113}, C_{123}, C_{113}, C_{223}, C_{233}, C_{133}, C_{133}, C_{333}, C_{111}, C_{112}, C_{122}, C_{222}$	D_{3333}	

Table S5. Atomic coordinates, displacement parameters (Å²), site-occupancy factors (SOFs) and bond valence sums (BVS, v.u.) in the structure of $Ag_3B_6O_{10}I$ at 25 °C.

Atom	Wyckoff site	SOF	*x*	*y*	*z*	U_{eq}	BVS
I1	4*c*	1	0.41402(3)	0.25	0.35880(5)	0.02853(10)	1.408(2)
Ag1	4*c*	1	0.11340(4)	0.25	0.01804(10)	0.03117(12)	0.906(2)
Ag2	8*d*	1	0.03929(7)	0.39716(12)	0.32058(7)	0.0778(4)	1.054(2)
O1	8*d*	1	0.57971(15)	−0.1290(2)	0.1725(2)	0.0157(5)	2.035(10)
O2	4*c*	1	0.4222(2)	−0.25	0.2229(3)	0.0152(7)	1.987(17)
O3	8*d*	1	0.82528(15)	−0.12734(19)	0.4749(2)	0.0137(5)	1.952(11)
O4	4*c*	1	0.73426(18)	−0.25	0.2637(3)	0.0072(6)	2.032(11)
O5	8*d*	1	0.24570(15)	−0.09411(19)	0.4563(2)	0.0135(5)	2.038(12)
O6	8*d*	1	0.71023(16)	−0.00559(20)	0.3036(2)	0.0148(5)	1.977(12)

B1	8*d*	1	0.2356(2)	0.0140(3)	0.5577(3)	0.0109(7)	3.053(16)
B2	8*d*	1	0.6938(2)	−0.1169(3)	0.1944(3)	0.0090(6)	3.101(14)
B3	4*c*	1	0.5261(3)	−0.25	0.1870(5)	0.0111(10)	3.066(17)
B4	4*c*	1	0.3289(3)	−0.25	0.1251(5)	0.0091(9)	3.042(16)

Table S6. Atomic coordinates, displacement parameters (Å^2), site-occupancy factors (SOFs) and bond valence sums (BVS, v.u.) in the structure of $Na_3B_6O_{10}I$ at 25 °C.

Atom	Wyckoff site	SOF	*x*	*y*	*z*	U_{eq}	BVS
I1	4*c*	1	0.444920(15)	0.25	0.22631(3)	0.01994(6)	0.9475(7)
Na1	4*b*	1	0.5	0	0	0.0265(4)	1.0089(9)
Na2	4*a*	1	0.5	0	0.5	0.0222(3)	1.0268(12)
Na3	4*c*	1	0.79866(11)	−0.25	0.6249(3)	0.0442(6)	0.8030(14)
O1	8*d*	1	0.55158(9)	−0.12960(13)	0.26018(16)	0.0097(3)	2.156(7)
O2	4*c*	1	0.39275(15)	−0.25	0.2545(3)	0.0171(5)	1.954(12)
O3	8*d*	1	0.71387(10)	−0.09486(12)	0.41374(16)	0.0132(3)	2.056(8)
O4	4*c*	1	0.70895(12)	−0.25	0.1782(2)	0.0072(4)	2.131(8)
O5	8*d*	1	0.33086(10)	−0.12990(13)	0.50483(17)	0.0152(4)	2.010(8)
O6	8*d*	1	0.68627(9)	−0.01148(12)	0.12220(16)	0.0114(3)	2.044(8)
B1	8*d*	1	0.26822(15)	−0.01980(19)	0.4927(2)	0.0104(5)	3.110(11)
B2	8*d*	1	0.66527(15)	−0.11843(18)	0.2470(2)	0.0082(4)	3.147(9)
B3	4*c*	1	0.4986(2)	−0.25	0.2609(3)	0.0092(6)	3.088(12)
B4	4*c*	1	0.3184(2)	−0.25	0.3959(4)	0.0105(6)	3.123(11)

Table S7. Atomic coordinates, displacement parameters (Å^2), site-occupancy factors (SOFs) and bond valence sums (BVS, v.u.) in the structure of $Ag_3B_6O_{10}I$ at 110 °C.

Atom	Wyckoff site	SOF	*x*	*y*	*z*	U_{eq}	BVS
I1	4*c*	1	0.43235(20)	0.25	0.3457(2)	0.0687(5)	1.507(13)
Ag1	8*d*	0.808(5)	0.10937(16)	0.25	0.0073(4)	0.0694(13)	1.11(1)
Ag2	8*d*	0.359(7)	0.4945(4)	0.0736(4)	0.1054(13)	0.091(2)	0.89(2)
Ag3	4*c*	0.5522	0.6762(6)	0.25	0.2344(5)	0.1015(15)	0.76(3)
Ag4	8*d*	0.1685	0.029(3)	0.031(3)	−0.044(3)	0.101(9)	0.61(2)
Ag5	8*d*	0.292(7)	0.5511(9)	0.1202(8)	0.1802(7)	0.107(3)	1.47(4)
O1	8*d*	1	0.5802(3)	−0.1274(4)	0.1781(6)	0.0258(15)	2.02(3)
O2	4*c*	1	0.4223(5)	−0.25	0.2234(8)	0.0215(19)	2.07(5)
O3	8*d*	1	0.8273(4)	−0.1264(4)	0.4733(5)	0.0208(14)	2.03(3)
O4	4*c*	1	0.7348(5)	−0.25	0.2672(7)	0.0106(16)	1.97(3)
O5	8*d*	1	0.2448(4)	−0.0932(4)	0.4493(5)	0.0193(14)	2.03(3)
O6	8*d*	1	0.7132(4)	−0.0004(4)	0.3062(5)	0.0231(15)	1.96(3)
B1	8*d*	1	0.2332(6)	0.0130(6)	0.5566(8)	0.016(2)	3.07(4)
B2	8*d*	1	0.6933(6)	−0.1127(6)	0.1965(8)	0.0127(19)	3.13(3)
B3	4*c*	1	0.5268(9)	−0.25	0.1950(11)	0.013(3)	3.10(5)
B4	4*c*	1	0.3305(8)	−0.25	0.1287(12)	0.013(3)	3.11(4)

Table S8. Atomic coordinates, displacement parameters (Å^2), site-occupancy factors (SOFs) and bond valence sums (BVS, v.u.) in the structure of $Ag_3B_6O_{10}I$ at 120 °C.

Atom	Wyckoff site	SOF	*x*	*y*	*z*	U_{eq}	BVS
I1	4*c*	1	0.43229(19)	0.25	0.3457(2)	0.0669(4)	1.478(12)
Ag1	4*c*	0.780(4)	0.10989(16)	0.25	0.0069(4)	0.0625(6)	1.11(1)
Ag2	8*d*	0.349(8)	0.4950(4)	0.0742(4)	0.1081(15)	0.084(2)	0.90(2)
Ag3	4*c*	0.537(5)	0.6756(6)	0.25	0.2365(6)	0.0954(16)	0.75(3)
Ag4	8*d*	0.225(3)	0.0326(6)	0.0350(6)	−0.0560(7)	0.116(3)	0.62(2)
Ag5	8*d*	0.267(9)	0.5512(11)	0.1207(11)	0.1791(8)	0.103(4)	1.46(4)
O1	8*d*	1	0.5799(4)	−0.1275(4)	0.1793(6)	0.0246(15)	2.03(3)
O2	4*c*	1	0.4228(5)	−0.25	0.2231(8)	0.021(2)	2.04(4)
O3	8*d*	1	0.8277(4)	−0.1266(4)	0.4738(6)	0.0221(15)	2.00(3)
O4	4*c*	1	0.7348(5)	−0.25	0.2680(7)	0.0110(17)	2.01(3)
O5	8*d*	1	0.2453(4)	−0.0929(4)	0.4500(6)	0.0191(14)	2.02(3)
O6	8*d*	1	0.7128(4)	−0.0003(4)	0.3069(6)	0.0233(15)	1.98(3)
B1	8*d*	1	0.2341(6)	0.0128(6)	0.5559(9)	0.017(2)	3.08(4)
B2	8*d*	1	0.6934(6)	−0.1129(7)	0.1984(9)	0.0133(19)	3.09(4)
B3	4*c*	1	0.5274(9)	−0.25	0.1936(11)	0.011(3)	3.15(5)
B4	4*c*	1	0.3297(8)	−0.25	0.1279(12)	0.013(3)	3.10(4)

Table S9. Atomic coordinates, displacement parameters (Å^2), site-occupancy factors (SOFs) and bond valence sums (BVS, v.u.) in the structure of $Ag_3B_6O_{10}I$ at 140 °C.

Atom	Wyckoff site	SOF	*x*	*y*	*z*	U_{eq}	BVS
I1	4*c*	1	0.43284(19)	0.25	0.3456(2)	0.0728(6)	1.489(13)
Ag1	4*c*	0.799(6)	0.10982(17)	0.25	0.0072(5)	0.0836(19)	1.19(2)
Ag2	8*d*	0.351(7)	0.4993(6)	0.0753(3)	0.1102(14)	0.087(2)	0.94(3)
Ag3	4*c*	0.532(5)	0.6758(6)	0.25	0.2373(6)	0.0982(15)	0.82(1)
Ag4	8*d*	0.234(3)	0.0338(5)	0.0376(6)	−0.0548(7)	0.118(3)	0.64(3)
Ag5	8*d*	0.249(9)	0.5514(12)	0.1222(13)	0.1792(8)	0.118(5)	1.54(2)
O1	8*d*	1	0.5799(3)	−0.1272(4)	0.1797(6)	0.0276(15)	2.06(3)
O2	4*c*	1	0.4227(4)	−0.25	0.2242(8)	0.0243(19)	2.03(4)
O3	8*d*	1	0.8278(3)	−0.1271(4)	0.4736(5)	0.0227(13)	1.99(2)
O4	4*c*	1	0.7344(4)	−0.25	0.2676(7)	0.0120(16)	2.02(3)
O5	8*d*	1	0.2454(4)	−0.0931(4)	0.4498(5)	0.0215(13)	1.99(3)
O6	8*d*	1	0.7121(4)	−0.0002(4)	0.3072(5)	0.0237(14)	2.01(3)
B1	8*d*	1	0.2346(6)	0.0128(6)	0.5562(8)	0.0167(19)	3.06(4)
B2	8*d*	1	0.6928(5)	−0.1131(7)	0.2001(8)	0.0141(18)	3.10(3)
B3	4*c*	1	0.5275(8)	−0.25	0.1941(11)	0.015(3)	3.13(4)
B4	4*c*	1	0.3294(7)	−0.25	0.1273(11)	0.013(3)	3.10(4)

Table S10. Atomic coordinates, displacement parameters (Å^2), site-occupancy factors (SOFs) and bond valence sums (BVS, v.u.) in the structure of $Ag_3B_6O_{10}I$ at 300 °C.

Atom	Wyckoff site	SOF	*x*	*y*	*z*	U_{eq}	BVS
I1	4*c*	1	0.43526(19)	0.25	0.3434(3)	0.0893(7)	1.58(3)
Ag1	4*c*	0.696(8)	0.1120(5)	0.25	0.0093(10)	0.120(4)	1.27(3)
Ag2	8*d*	0.349(12)	0.4989(10)	0.0660(11)	0.108(3)	0.125(4)	0.95(2)
Ag3	4*c*	0.572(10)	0.6797(7)	0.25	0.2505(10)	0.132(5)	0.66(3)
Ag4	8*d*	0.292(4)	0.0249(13)	0.0216(17)	−0.0690(11)	0.177(5)	0.52(2)
Ag5	8*d*	0.225(14)	0.548(3)	0.137(3)	0.1743(14)	0.202(12)	1.87(4)
O1	8*d*	1	0.5796(4)	−0.1252(4)	0.1821(6)	0.0377(18)	2.04(3)
O2	4*c*	1	0.4230(5)	−0.25	0.2224(9)	0.036(2)	1.95(5)
O3	8*d*	1	0.8277(4)	−0.1271(5)	0.4752(6)	0.0348(17)	1.95(3)
O4	4*c*	1	0.7352(4)	−0.25	0.2671(7)	0.0157(18)	2.10(3)
O5	8*d*	1	0.2440(4)	−0.0919(4)	0.4501(6)	0.0322(17)	1.94(3)
O6	8*d*	1	0.7119(4)	−0.0021(4)	0.3070(5)	0.0346(17)	2.00(3)
B1	8*d*	1	0.2336(6)	0.0129(7)	0.5565(10)	0.027(3)	3.07(4)
B2	8*d*	1	0.6924(6)	−0.1151(7)	0.2015(10)	0.022(2)	3.12(4)
B3	4*c*	1	0.5286(10)	−0.25	0.1898(14)	0.029(4)	3.04(5)
B4	4*c*	1	0.3289(8)	−0.25	0.1286(12)	0.014(3)	3.08(4)

Table S11. Atomic coordinates, displacement parameters (Å²), site-occupancy factors (SOFs) and bond valence sums (BVS, v.u.) in the structure of $Ag_3B_6O_{10}I$ at 400 °C.

Atom	Wyckoff site	SOF	*x*	*y*	*z*	U_{eq}	BVS
I1	4*c*	1	0.43690(19)	0.25	0.3427(3)	0.0922(6)	1.500(14)
Ag1	4*c*	0.625(5)	0.1104(3)	0.25	0.0086(8)	0.125(3)	1.14(3)
Ag2	8*d*	0.320(9)	0.4947(4)	0.0674(5)	0.1233(13)	0.0972(19)	1.01(3)
Ag3	4*c*	0.379(17)	0.6960(10)	0.25	0.2709(13)	0.126(4)	0.76(2)
Ag4	8*d*	0.305(4)	0.0364(5)	0.0263(8)	−0.0511(7)	0.174(4)	0.63(3)
Ag5	8*d*	0.307(14)	0.5984(11)	0.1745(11)	0.2004(9)	0.290(12)	1.38(2)
Ag6	4b	0.13(4)	0.5	0	0	0.29(4)	0.97(4)
O1	8*d*	1	0.5798(3)	−0.1261(4)	0.1833(5)	0.0376(15)	2.03(2)
O2	4*c*	1	0.4226(5)	−0.25	0.2228(8)	0.038(2)	1.95(4)
O3	8*d*	1	0.8279(4)	−0.1277(4)	0.4741(5)	0.0344(14)	2.05(3)
O4	4*c*	1	0.7355(4)	−0.25	0.2670(6)	0.0187(16)	2.02(3)
O5	8*d*	1	0.2428(4)	−0.0921(4)	0.4507(5)	0.0319(14)	1.99(3)
O6	8*d*	1	0.7121(4)	−0.0031(4)	0.3092(5)	0.0355(15)	2.06(3)
B1	8*d*	1	0.2327(6)	0.0135(6)	0.5552(7)	0.023(2)	3.12(4)
B2	8*d*	1	0.6929(5)	−0.1132(6)	0.2015(7)	0.0193(18)	3.13(3)
B3	4*c*	1	0.5284(8)	−0.25	0.1929(11)	0.024(3)	3.06(4)
B4	4*c*	1	0.3297(7)	−0.25	0.1266(10)	0.014(2)	3.14(4)

Table S12. Anisotropic parameters of atomic displacements in the structure of $Ag_3B_6O_{10}I$ at 25 °C.

Atom	U_{11}	U_{22}	U_{33}	U_{12}	U_{13}	U_{23}
I1	0.01617(13)	0.0442(2)	0.02521(16)	0	0.00534(10)	0
Ag1	0.02213(17)	0.0408(2)	0.0305(2)	0	0.01039(14)	0
Ag2	0.0910(5)	0.0541(6)	0.0882(8)	−0.0515(4)	−0.0198(4)	−0.0034(4)
O1	0.0099(8)	0.0124(9)	0.0249(10)	−0.0002(6)	−0.0030(7)	0.0039(8)
O2	0.0091(11)	0.0242(14)	0.0123(12)	0	−0.0012(9)	0
O3	0.0143(8)	0.0126(8)	0.0142(9)	0.0027(7)	−0.0056(7)	−0.0035(7)
O4	0.0069(10)	0.0077(10)	0.0068(10)	0	−0.0010(8)	0
O5	0.0178(9)	0.0117(8)	0.0110(9)	0.0032(7)	−0.0035(7)	−0.0037(7)
O6	0.0219(9)	0.0104(8)	0.0123(9)	0.0039(7)	−0.0066(7)	−0.0024(7)
B1	0.0132(12)	0.0095(12)	0.0098(12)	0.0004(9)	−0.0003(9)	−0.0013(9)
B2	0.0075(10)	0.0091(11)	0.0106(11)	0.0003(9)	−0.0016(9)	0.0013(9)
B3	0.0083(15)	0.0140(18)	0.0109(17)	0	−0.0032(13)	0
B4	0.0081(15)	0.0079(15)	0.0112(17)	0	0.0008(12)	0

Table S13. Third−order anharmonic thermal parameters in the structure of $Ag_3B_6O_{10}I$ obtained using Gram−Charlie model at 25 °C.

Atom	C_{111}	C_{112}	C_{113}	C_{122}	C_{123}	C_{133}	C_{222}	C_{223}	C_{233}	C_{333}
I1	0	0	0	0.00081(6)	0	0	0	0.00082(10)	0	0
Ag1	0	0	0.00027(5)	−0.00143(7)	0	0.00095(8)	0	−0.00095(12)	0	0.0024(2)
Ag2	0	0	0	0.0014(2)	0.00378(11)	−0.0221(3)	−0.0027(6)	−0.0068(2)	0.0207(3)	0

Table S14. Fourth−order anharmonic thermal parameters in the structure of $Ag_3B_6O_{10}I$ obtained using Gram−Charlie model at 25 °C.

Atom	D_{1111}	D_{1112}	D_{1113}	D_{1122}	D_{1123}	D_{1133}	D_{1222}	D_{1223}	D_{1233}	D_{1333}	D_{2222}	D_{2223}	D_{2233}	D_{2333}	D_{3333}
Ag2	0	0	0	0.00048(5)	−0.00041(6)	0.00303(13)	−0.00100(11)	0.00078(8)	−0.00301(12)	0.0009(3)	0.0021(2)	−0.00122(16)	0.00331(18)	−0.0027(3)	0.0161(9)

Table S15. Fifth−order anharmonic thermal parameters in the structure of $Ag_3B_6O_{10}I$ obtained using Gram−Charlie model at 25 °C.

Atom	E_{11111}	E_{11112}	E_{11113}	E_{11122}	E_{11123}	E_{11133}	E_{11222}	E_{11223}	E_{11233}	E_{11333}	E_{12222}	E_{12223}	E_{12233}	E_{12333}	E_{13333}	E_{22222}	E_{22223}	E_{22233}	E_{22333}	E_{23333}	E_{33333}
Ag2	0.00113(5)	−0.00066(5)	0	0.00059(5)	0	0	−0.00048(6)	0	0	0	0.00052(9)	0	0	0	0	−0.0008(2)	0	0	0	0	0

Table S16. Anisotropic parameters of atomic displacements in the structure of $Na_3B_6O_{10}I$ at 25 °C.

Atom	U_{11}	U_{22}	U_{33}	U_{12}	U_{13}	U_{23}
I1	0.02212(10)	0.01872(10)	0.01897(10)	0	−0.00097(7)	0
Na1	0.0341(7)	0.0222(6)	0.0233(6)	0.0093(5)	−0.0093(5)	−0.0015(5)
Na2	0.0189(6)	0.0247(6)	0.0229(6)	−0.0017(5)	0.0036(5)	−0.0103(5)
Na3	0.0272(7)	0.0199(7)	0.0854(13)	0	−0.0115(8)	0
O1	0.0069(5)	0.0078(5)	0.0144(6)	0.0000(4)	0.0029(4)	−0.0012(4)
O2	0.0059(8)	0.0206(9)	0.0248(10)	0	0.0016(7)	0
O3	0.0190(6)	0.0094(5)	0.0113(6)	0.0005(5)	−0.0046(5)	−0.0033(4)
O4	0.0065(7)	0.0064(7)	0.0088(7)	0	0.0018(6)	0
O5	0.0129(6)	0.0108(6)	0.0218(7)	0.0026(5)	−0.0086(5)	−0.0053(5)
O6	0.0134(6)	0.0085(5)	0.0122(5)	0.0023(4)	0.0048(4)	0.0028(4)
B1	0.0095(8)	0.0109(8)	0.0107(8)	−0.0011(6)	−0.0011(6)	−0.0012(6)
B2	0.0077(7)	0.0065(7)	0.0103(8)	0.0001(6)	0.0008(6)	0.0000(5)
B3	0.0084(10)	0.0100(11)	0.0092(11)	0	0.0004(8)	0
B4	0.0083(11)	0.0069(11)	0.0162(12)	0	−0.0017(9)	0

Table S17. Anisotropic parameters of atomic displacements in the structure of $Ag_3B_6O_{10}I$ at 110 °C.

	U_{11}	U_{22}	U_{33}	U_{12}	U_{13}	U_{23}
I1	0.0546(9)	0.0953(10)	0.0564(10)	0	−0.0039(7)	0
Ag1	0.0403(11)	0.098(4)	0.0698(12)	0	0.0294(8)	0
Ag2	0.0444(18)	0.0477(14)	0.179(5)	0.0202(13)	0.0108(17)	0.0230(12)
Ag3	0.202(4)	0.0385(11)	0.0646(16)	0	0.011(2)	0
Ag4	0.111(19)	0.103(10)	0.087(16)	0.075(10)	−0.016(10)	−0.012(9)
Ag5	0.148(8)	0.117(4)	0.056(3)	0.107(5)	0.040(4)	0.018(3)
O1	0.008(2)	0.022(2)	0.047(3)	0.0004(19)	−0.008(2)	0.0067(19)
O2	0.008(3)	0.039(3)	0.017(3)	0	−0.002(3)	0
O3	0.018(3)	0.021(2)	0.024(3)	0.0046(19)	−0.010(2)	−0.0114(18)
O4	0.010(3)	0.012(3)	0.010(3)	0	−0.002(2)	0
O5	0.026(3)	0.0134(19)	0.019(2)	0.0058(18)	−0.002(2)	−0.0079(17)
O6	0.031(3)	0.021(2)	0.018(2)	0.005(2)	−0.009(2)	−0.0032(18)
B1	0.020(4)	0.017(3)	0.012(3)	−0.003(3)	0.002(3)	0.003(3)
B2	0.009(3)	0.006(3)	0.023(4)	0.002(3)	−0.006(3)	0.002(3)
B3	0.015(5)	0.016(5)	0.009(5)	0	−0.003(4)	0
B4	0.006(5)	0.018(5)	0.016(5)	0	0.003(4)	0

Table S18. Third−order anharmonic thermal parameters in the structure of $Ag_3B_6O_{10}I$ obtained using Gram−Charlie model at 110 °C.

Atom	C_{111}	C_{112}	C_{113}	C_{122}	C_{123}	C_{133}	C_{222}	C_{223}	C_{233}	C_{333}
I1	0.0043(3)	0	0	0.0038(4)	0	0.0068(4)	0	−0.0033(5)	0	−0.0087(10)
Ag1	0	0	0.0031(3)	−0.0087(6)	0	0.0073(6)	0	−0.0065(9)	0	0.0237(17)
Ag2	0	0.0018(5)	0.0046(10)	0	0.0059(8)	0.002(3)	−0.0033(12)	0	0	0.149(15)
Ag3	0.029(3)	0	−0.0216(16)	−0.0057(8)	0	−0.0116(14)	0	0	0	0.018(2)
Ag4	-0.014(5)	-0.014(3)	0	-0.013(3)	0.014(2)	0	0	0.035(6)	-0.020(6)	0.030(13)

Table S19. Fourth−order anharmonic thermal parameters in the structure of $Ag_3B_6O_{10}I$ obtained using Gram−Charlie model at 110 °C.

Atom	D_{1111}	D_{1112}	D_{1113}	D_{1122}	D_{1123}	D_{1133}	D_{1222}	D_{1223}	D_{1233}	D_{1333}	D_{2222}	D_{2223}	D_{2233}	D_{2333}	D_{3333}
I1	0	0	0.00056(17)	0	0	0.0008(2)	0	0	0	0	0	0	0.0019(4)	0	0
Ag1	0	0	0	0.0007(3)	0	0	0	0	0	0	0.015(3)	0	0	0	0
Ag2	0	0	0	0	0	0	0	0	0	0	0	0	0	0	0.27(3)

Table S20. Anisotropic parameters of atomic displacements in the structure of $Ag_3B_6O_{10}I$ at 120 °C.

Atom	U_{11}	U_{22}	U_{33}	U_{12}	U_{13}	U_{23}
I1	0.0528(8)	0.0940(8)	0.0538(7)	0	−0.0064(5)	0
Ag1	0.0384(9)	0.0766(11)	0.0725(13)	0	0.0302(8)	0
Ag2	0.0417(19)	0.0442(15)	0.167(5)	0.0185(14)	0.011(2)	0.0214(12)
Ag3	0.190(4)	0.0350(13)	0.0616(18)	0	0.0112(19)	0
Ag4	0.139(7)	0.105(4)	0.105(5)	0.067(4)	−0.010(4)	0.012(3)
Ag5	0.141(9)	0.111(5)	0.057(4)	0.102(6)	0.046(4)	0.020(3)
O1	0.009(2)	0.020(2)	0.045(3)	0.0033(19)	−0.007(2)	0.0064(19)
O2	0.007(3)	0.038(4)	0.019(3)	0	−0.006(3)	0
O3	0.020(3)	0.019(2)	0.027(3)	0.0047(19)	−0.010(2)	−0.0119(19)
O4	0.009(3)	0.009(3)	0.014(3)	0	−0.004(3)	0
O5	0.023(3)	0.013(2)	0.021(3)	0.0044(18)	−0.003(2)	−0.0053(18)
O6	0.026(3)	0.018(2)	0.026(3)	0.0038(19)	−0.008(2)	−0.0016(18)
B1	0.019(4)	0.013(3)	0.018(4)	−0.004(3)	0.005(3)	0.006(3)
B2	0.009(3)	0.010(3)	0.021(4)	0.003(3)	−0.004(3)	0.004(3)
B3	0.015(5)	0.016(5)	0.002(4)	0	0.001(4)	0
B4	0.002(5)	0.018(5)	0.017(5)	0	0.004(4)	0

Table S21. Third−order anharmonic thermal parameters in the structure of $Ag_3B_6O_{10}I$ obtained using Gram−Charlie model at 120 °C.

Atom	C_{111}	C_{112}	C_{113}	C_{122}	C_{123}	C_{133}	C_{222}	C_{223}	C_{233}	C_{333}
I1	0.0034(3)	0	0	0.0032(4)	0	0.0065(4)	0	−0.0033(5)	0	−0.0067(10)
Ag1	0	0	0.0030(3)	−0.0071(4)	0	0.0079(6)	0	−0.0069(7)	0	0.0249(18)
Ag2	0	0.0022(5)	0.0045(10)	0	0.0056(8)	0.006(3)	−0.0021(12)	0	0	0.171(14)
Ag3	0.024(2)	0	−0.0214(15)	−0.0059(8)	0	−0.0094(13)	0	−0.0003(9)	0	0.026(3)

Table S22. Fourth−order anharmonic thermal parameters in the structure of $Ag_3B_6O_{10}I$ obtained using Gram−Charlie model at 120 °C.

Atom	D_{1111}	D_{1112}	D_{1113}	D_{1122}	D_{1123}	D_{1133}	D_{1222}	D_{1223}	D_{1233}	D_{1333}	D_{2222}	D_{2223}	D_{2233}	D_{2333}	D_{3333}
Ag2	0	0	0	0	0	0	0	0	0	0	0	0	0	0	0.20(3)

Table S23. Anisotropic parameters of atomic displacements in the structure of $Ag_3B_6O_{10}I$ at 140 °C.

Atom	U_{11}	U_{22}	U_{33}	U_{12}	U_{13}	U_{23}
I1	0.0547(10)	0.1004(12)	0.0631(10)	0	−0.0031(7)	0
Ag1	0.0463(13)	0.118(5)	0.086(2)	0	0.0295(9)	0
Ag2	0.053(3)	0.0456(14)	0.164(5)	0.0209(15)	0.022(3)	0.0228(12)
Ag3	0.191(4)	0.0356(12)	0.0680(18)	0	0.010(2)	0
Ag4	0.129(6)	0.105(4)	0.121(5)	0.063(4)	−0.012(4)	0.010(3)
Ag5	0.178(12)	0.121(7)	0.055(4)	0.118(8)	0.052(5)	0.023(3)
O1	0.011(2)	0.023(2)	0.048(3)	−0.0005(18)	−0.007(2)	0.0100(19)
O2	0.007(3)	0.040(3)	0.026(3)	0	−0.005(3)	0
O3	0.020(2)	0.021(2)	0.028(3)	0.0018(18)	−0.008(2)	−0.0089(17)
O4	0.012(3)	0.008(2)	0.016(3)	0	−0.004(2)	0
O5	0.025(2)	0.019(2)	0.020(2)	0.0067(18)	−0.0054(19)	−0.0034(17)
O6	0.030(3)	0.015(2)	0.026(2)	0.0045(18)	−0.006(2)	−0.0035(17)
B1	0.018(3)	0.011(3)	0.021(3)	−0.004(3)	0.000(3)	0.003(3)
B2	0.008(3)	0.012(3)	0.022(4)	−0.001(2)	−0.003(3)	0.001(3)
B3	0.017(5)	0.020(5)	0.008(4)	0	−0.002(4)	0
B4	0.005(4)	0.015(4)	0.018(5)	0	0.005(4)	0

Table S24. Third−order anharmonic thermal parameters in the structure of $Ag_3B_6O_{10}I$ obtained using Gram−Charlie model at 140 °C.

Atom	C_{111}	C_{112}	C_{113}	C_{122}	C_{123}	C_{133}	C_{222}	C_{223}	C_{233}	C_{333}
I1	0.0037(3)	0	0	0.0032(4)	0	0.0067(4)	0	−0.0036(5)	0	−0.0070(10)
Ag1	0	0	0.0037(4)	−0.0104(8)	0	0.0104(7)	0	−0.0086(11)	0	0.034(2)
Ag2	0.0072(11)	0.0050(6)	0.0119(17)	0	0.0073(9)	0.024(4)	0	0	0	0.172(14)
Ag3	0.023(2)	0	−0.0229(14)	−0.0074(8)	0	−0.0107(14)	0	−0.0007(8)	0	0.028(3)

Table S25. Fourth−order anharmonic thermal parameters in the structure of $Ag_3B_6O_{10}I$ obtained using Gram−Charlie model at 140 °C.

Atom	D_{1111}	D_{1112}	D_{1113}	D_{1122}	D_{1123}	D_{1133}	D_{1222}	D_{1223}	D_{1233}	D_{1333}	D_{2222}	D_{2223}	D_{2233}	D_{2333}	D_{3333}
I1	0	0	0.00068(16)	−0.00062(19)	0	0.0008(2)	0	0	0	0	0	0	0.0041(5)	0	0
Ag1	0	0	0	0.0011(3)	0	0.0015(3)	0	0	0	0	0.025(5)	0	0.0035(10)	0	0
Ag2	0	0	0	0	0	0	0	0	0	0	0	0	0	0	0.16(3)

Table S26. Anisotropic parameters of atomic displacements in the structure of $Ag_3B_6O_{10}I$ at 300 °C.

Atom	U_{11}	U_{22}	U_{33}	U_{12}	U_{13}	U_{23}
I1	0.0668(11)	0.1191(13)	0.0819(12)	0	−0.0068(7)	0
Ag1	0.077(5)	0.154(8)	0.128(8)	0	0.056(5)	0
Ag2	0.079(7)	0.100(9)	0.195(6)	0.009(5)	0.002(5)	0.032(6)
Ag3	0.242(12)	0.063(5)	0.089(8)	0	−0.018(6)	0
Ag4	0.220(10)	0.186(7)	0.126(8)	0.120(7)	−0.026(6)	0.024(6)
Ag5	0.33(3)	0.209(17)	0.070(7)	0.211(19)	0.081(11)	0.033(8)
O1	0.020(3)	0.034(2)	0.060(4)	0.006(2)	−0.004(3)	0.016(2)
O2	0.016(4)	0.051(4)	0.041(4)	0	0.000(4)	0
O3	0.035(3)	0.042(2)	0.027(3)	−0.001(2)	−0.016(3)	−0.014(2)
O4	0.014(3)	0.025(3)	0.008(3)	0	−0.004(3)	0
O5	0.045(3)	0.033(3)	0.019(3)	0.003(2)	−0.007(2)	−0.007(2)
O6	0.049(3)	0.025(2)	0.030(3)	0.013(2)	−0.011(2)	0.002(2)
B1	0.019(4)	0.027(4)	0.035(5)	0.002(3)	−0.002(4)	0.007(4)
B2	0.019(4)	0.020(3)	0.028(5)	0.000(3)	0.005(4)	0.005(3)
B3	0.030(7)	0.033(6)	0.024(7)	0	−0.008(6)	0
B4	0.018(6)	0.014(4)	0.009(5)	0	0.001(4)	0

Table S27. Third−order anharmonic thermal parameters in the structure of $Ag_3B_6O_{10}I$ obtained using Gram−Charlie model at 300 °C.

Atom	C_{111}	C_{112}	C_{113}	C_{122}	C_{123}	C_{133}	C_{222}	C_{223}	C_{233}	C_{333}
I1	0.0031(4)	0	−0.0013(4)	0.0050(4)	0	0.0079(6)	0	−0.0065(8)	0	−0.0144(16)
Ag1	0.0030(10)	0	0.0096(17)	−0.0197(16)	0	0.028(4)	0	−0.021(2)	0	0.071(11)
Ag2	0.007(2)	0	0.013(2)	0	0.008(3)	0.018(6)	−0.006(6)	−0.015(5)	−0.050(9)	0.23(3)
Ag3	0.033(4)	0	−0.021(3)	−0.0134(18)	0	0	0	0	0	0.046(8)
Ag4	−0.046(6)	−0.035(5)	0.010(5)	−0.018(5)	0.018(5)	0.007(4)	−0.003(7)	0.011(8)	−0.051(7)	−0.137(13)
Ag5	0	0.036(6)	0	0.087(12)	0	−0.018(4)	0.20(2)	0	−0.028(5)	0

Table S28. Fourth−order anharmonic thermal parameters in the structure of $Ag_3B_6O_{10}I$ obtained using Gram−Charlie model at 300 °C.

Atom	D_{1111}	D_{1112}	D_{1113}	D_{1122}	D_{1123}	D_{1133}	D_{1222}	D_{1223}	D_{1233}	D_{1333}	D_{2222}	D_{2223}	D_{2233}	D_{2333}	D_{3333}
I1	0	0	0	−0.0015(2)	0	0.0020(3)	0	0	0	0	0	0	0.0060(7)	0	0
Ag1	0.0014(8)	0	0.0029(10)	0.0005(7)	0	0.0066(17)	0	0.0003(10)	0	0.004(3)	0.032(8)	0	0.002(2)	0	0.004(8)
Ag2	0.0036(12)	0.0003(9)	−0.0001(10)	−0.0006(7)	−0.0005(8)	0.003(2)	−0.0025(15)	−0.0058(19)	−0.009(3)	−0.033(8)	0.013(7)	0.017(7)	0.029(7)	0.028(12)	0.18(5)
Ag3	0.014(5)	0	−0.008(2)	0.0061(15)	0	−0.0055(18)	0	0.0020(10)	0	0.003(2)	0.001(2)	0	0.0021(13)	0	0.001(6)

Table S29. Anisotropic parameters of atomic displacements in the structure of $Ag_3B_6O_{10}I$ at 400 °C.

Atom	U_{11}	U_{22}	U_{33}	U_{12}	U_{13}	U_{23}
I1	0.0687(10)	0.1229(12)	0.0849(11)	0	−0.0059(6)	0
Ag1	0.0704(16)	0.185(8)	0.120(3)	0	0.0507(18)	0
Ag2	0.067(3)	0.064(3)	0.160(4)	0.0258(18)	0.0074(19)	0.004(2)
Ag3	0.211(11)	0.042(3)	0.127(6)	0	−0.061(6)	0
Ag4	0.157(6)	0.163(5)	0.203(7)	0.077(4)	−0.021(4)	0.008(3)
Ag5	0.46(3)	0.251(14)	0.160(15)	0.262(17)	0.142(18)	0.095(10)
Ag6	0.054(13)	0.56(8)	0.27(7)	−0.08(3)	−0.07(2)	0.32(6)
O1	0.024(2)	0.030(2)	0.059(3)	−0.003(2)	−0.007(2)	0.018(2)
O2	0.012(3)	0.057(3)	0.044(4)	0	−0.004(3)	0
O3	0.036(3)	0.040(2)	0.028(3)	0.007(2)	−0.017(2)	−0.0136(19)
O4	0.017(3)	0.019(2)	0.021(3)	0	−0.003(3)	0
O5	0.044(3)	0.030(2)	0.022(2)	0.004(2)	−0.011(2)	−0.0089(18)
O6	0.050(3)	0.0227(19)	0.034(3)	0.018(2)	−0.014(2)	−0.0014(18)
B1	0.025(4)	0.029(3)	0.016(3)	0.001(3)	0.004(3)	0.003(3)
B2	0.013(3)	0.022(3)	0.023(4)	−0.008(3)	−0.007(3)	0.003(3)
B3	0.019(5)	0.031(5)	0.023(5)	0	−0.007(4)	0
B4	0.012(4)	0.012(3)	0.019(5)	0	0.004(4)	0

Table S30. Third−order anharmonic thermal parameters in the structure of $Ag_3B_6O_{10}I$ obtained using Gram−Charlie model at 400 °C.

Atom	C_{111}	C_{112}	C_{113}	C_{122}	C_{123}	C_{133}	C_{222}	C_{223}	C_{233}	C_{333}
I1	0.0028(3)	0	−0.0014(3)	0.0052(4)	0	0.0077(5)	0	−0.0078(7)	0	−0.0184(14)
Ag1	0	0	0.0077(8)	−0.031(2)	0	0.024(2)	0	−0.030(2)	0	0.070(6)
Ag2	0	0	0.0107(12)	0	0.0063(11)	0	0	0	−0.035(4)	0.262(15)
Ag3	0.031(5)	0	−0.019(4)	0	0	0	0	0	0	0.099(10)
Ag4	0	0	0	0	0	0	0	0	−0.089(7)	0
Ag5	0	0	0	0	0	0	0	0	0	0

Table S31. Fourth−order anharmonic thermal parameters in the structure of $Ag_3B_6O_{10}I$ obtained using Gram−Charlie model at 400 °C.

Atom	D_{1111}	D_{1112}	D_{1113}	D_{1122}	D_{1123}	D_{1133}	D_{1222}	D_{1223}	D_{1233}	D_{1333}	D_{2222}	D_{2223}	D_{2233}	D_{2333}	D_{3333}
I1	0	0	0	−0.0016(2)	0	0.0012(3)	0	0	0	0	0	0	0.0039(6)	0	0
Ag1	0	0	0	0	0	0	0	0	0	0	0.060(10)	0	0	0	0
Ag2	0	0	0	0	0	0	0	0	0	0	0	0	0	0	−0.003(16)
Ag3	−0.010(4)	0	0.021(4)	0	0	−0.020(4)	0	0	0	0.014(4)	0	0	0	0	−0.039(7)
Ag5	−0.32(4)	−0.28(4)	−0.15(3)	−0.27(4)	−0.14(2)	−0.089(19)	−0.30(4)	−0.14(2)	−0.105(19)	−0.088(16)	−0.35(4)	−0.16(3)	−0.112(19)	−0.079(16)	0

Table S32. I−Ag bond lengths in the $Ag_3B_6O_{10}I$ structure.

25 °C		110 °C		120 °C		140 °C		300 °C		400 °C	
Bond	Length (Å)	Bond	Length (Å)	Bond	Length (Å)	Bond	Length (Å)	Bond	Length (Å)	Bond	Length (Å)
I1−Ag1^{i}	2.7472(9)	I1−Ag1^{i}	2.582(3)	I1−Ag1^{i}	2.589(3)	I1−Ag1^{i}	2.582(4)	I1−Ag1^{i}	2.582(7)	I1−Ag1^{i}	2.550(5)
I1−Ag2^{i}	2.6230(10)	I1−Ag2	2.768(9)	I1−Ag2	2.749(10)	I1−Ag2	2.743(9)	I1−Ag2	2.788(17)	I1−Ag2	2.659(9)
I1−Ag2^{v}	2.6230(10)	I1−Ag2^{ii}	2.768(9)	I1−Ag2^{ii}	2.749(10)	I1−Ag2^{ii}	2.743(9)	I1−Ag2^{ii}	2.788(17)	I1−Ag2^{ii}	2.659(9)
		I1−Ag3	3.251(8)	I1−Ag3	3.238(8)	I1−Ag3	3.231(7)	I1−Ag3	3.221(9)	I1−Ag3	3.365(13)
		I1−Ag3^{iii}	3.336(8)	I1−Ag3^{iii}	3.347(8)	I1−Ag3^{iii}	3.351(8)	I1−Ag3^{iii}	3.360(9)	I1−Ag3^{iii}	3.225(13)
		I1−Ag4^{iv}	2.88(3)	I1−Ag4^{iv}	2.879(6)	I1−Ag4^{iv}	2.902(5)	I1−Ag4^{iv}	2.749(16)	I1−Ag4^{iv}	2.815(7)
		I1−Ag4^{i}	2.96(3)	I1−Ag4^{i}	3.009(6)	I1−Ag4^{i}	2.990(6)	I1−Ag4^{i}	3.126(14)	I1−Ag4^{i}	3.055(7)
		I1−Ag4^{v}	2.96(3)	I1−Ag4^{v}	3.009(6)	I1−Ag4^{v}	2.990(6)	I1−Ag4^{v}	3.126(14)	I1−Ag4^{v}	3.055(7)
		I1−Ag4^{vi}	2.88(3)	I1−Ag4^{vi}	2.879(6)	I1−Ag4^{vi}	2.902(5)	I1−Ag4^{vi}	2.749(16)	I1−Ag4^{vi}	2.815(7)
		I1−Ag5	2.412(9)	I1−Ag5	2.416(11)	I1−Ag5	2.405(13)	I1−Ag5	2.30(3)	I1−Ag5	2.497(13)
		I1−Ag5^{ii}	2.412(9)	I1−Ag5^{ii}	2.416(11)	I1−Ag5^{ii}	2.405(13)	I1−Ag5^{ii}	2.30(3)	I1−Ag5^{ii}	2.497(13)
										I1−Ag6	3.8527(19)
										I1−Ag6^{vii}	3.8527(19)

Symmetry codes: (i) x+1/2,−y+1/2,−z+1/2; (ii) x,−y+1/2,z; (iii) x−1/2,−y+1/2,−z+1/2; (iv) −x+1/2,−y,z+1/2; (v) x+1/2,y,−z+1/2; (vi) −x+1/2,y+1/2,z+1/2; (vii) −x+1,y+1/2,−z.

Table S33. Ag−O bond lengths in the $Ag_3B_6O_{10}I$ structure.

25 °C		110 °C		120 °C		140 °C		300 °C		400 °C	
Bond	Length (Å)	Bond	Length (Å)	Bond	Length (Å)	Bond	Length (Å)	Bond	Length (Å)	Bond	Length (Å)
Ag1−O2i	2.529(3)	Ag1−O2^{i}	2.456(7)	Ag1−O2^{i}	2.457(7)	Ag1−O2^{i}	2.450(8)	Ag1−O2^{i}	2.484(11)	Ag1−O2^{i}	2.463(10)
Ag1−O5^{i}	2.406(2)	Ag1−O5^{i}	2.437(5)	Ag1−O5^{i}	2.427(5)	Ag1−O5^{i}	2.425(5)	Ag1−O5^{i}	2.433(7)	Ag1−O5^{i}	2.459(5)
Ag1−O5^{ii}	2.406(2)	Ag1−O5^{ii}	2.437(5)	Ag1−O5^{ii}	2.427(5)	Ag1−O5^{ii}	2.425(5)	Ag1−O5^{ii}	2.433(7)	Ag1−O5^{ii}	2.459(5)
Ag2−O1^{iii}	2.309(2)	Ag2−O1	2.292(7)	Ag2−O1	2.288(7)	Ag2−O1	2.266(7)	Ag2−O1	2.191(13)	Ag2−O1	2.207(7)
Ag2−O3^{iv}	2.452(2)	Ag2−O1^{iii}	2.649(12)	Ag2−O1^{iii}	2.679(13)	Ag2−O1^{iii}	2.717(12)	Ag2−O1^{iii}	2.73(2)	Ag2−O1^{iii}	2.828(12)
Ag2−O6^{iii}	2.638(2)	Ag2−O3^{iv}	2.585(8)	Ag2−O3^{iv}	2.583(9)	Ag2−O3^{iv}	2.542(10)	Ag2−O3^{iv}	2.555(16)	Ag2−O3^{iv}	2.659(8)
		Ag2−O3^{v}	2.938(7)	Ag2−O3^{v}	2.950(7)	Ag2−O3^{v}	3.002(8)	Ag2−O3^{v}	2.948(14)	Ag2−O3^{v}	2.951(7)
		Ag3−O3^{iv}	2.521(6)	Ag3−O3^{iv}	2.531(7)	Ag3−O3^{iv}	2.537(6)	Ag3−O3^{iv}	2.624(9)	Ag3−O3^{iv}	2.795(11)
		Ag3−O3^{vi}	2.521(6)	Ag3−O3^{vi}	2.531(7)	Ag3−O3^{vi}	2.537(6)	Ag3−O3^{vi}	2.624(9)	Ag3−O3^{vi}	2.795(11)
		Ag3−O6	2.510(5)	Ag3−O6	2.506(5)	Ag3−O6	2.502(4)	Ag3−O6	2.492(5)	Ag3−O5^{vii}	2.913(11)
		Ag3−O6^{vii}	2.510(5)	Ag3−O6^{vii}	2.506(5)	Ag3−O6^{vii}	2.502(4)	Ag3−O6^{vii}	2.492(5)	Ag3−O5^{viii}	2.913(11)
		Ag4−O1^{i}	2.90(3)	Ag4−O1^{i}	2.816(8)	Ag4−O1^{i}	2.821(7)	Ag4−O1^{i}	2.693(13)	Ag3−O6	2.453(4)
		Ag4−O2^{i}	2.94(3)	Ag4−O2^{i}	2.841(7)	Ag4−O2^{i}	2.822(7)	Ag4−O2^{i}	2.893(15)	Ag3−O6^{ix}	2.453(4)
		Ag4−O5^{i}	2.94(3)	Ag4−O5^{i}	2.886(9)	Ag4−O5^{i}	2.863(8)	Ag4−O5^{i}	3.032(17)	Ag4−O1^{i}	2.864(8)
		Ag5−O1	2.391(9)	Ag5−O1	2.395(11)	Ag5−O1	2.406(13)	Ag5−O1	2.54(3)	Ag4−O2^{i}	2.924(8)
		Ag5−O3^{iv}	2.350(10)	Ag5−O3^{iv}	2.335(12)	Ag5−O3^{iv}	2.334(12)	Ag5−O3^{iv}	2.33(3)	Ag4−O5^{i}	2.891(8)
		Ag5−O6	2.598(11)	Ag5−O6	2.600(13)	Ag5−O6	2.598(15)	Ag5−O6	2.73(3)	Ag5−O1	2.891(11)
										Ag5−O3^{iv}	2.186(10)
										Ag5−O3^{vi}	2.857(11)
										Ag5−O6	2.420(13)
										Ag6−O1	2.218(4)
										Ag6−O1^{iii}	2.218(4)
										Ag6−O3^{iv}	2.525(4)
										Ag6−O3^{v}	2.525(4)

Symmetry codes for 25 °C: (i) −*x*+1/2,−*y*,*z*−1/2; (ii) −*x*+1/2,*y*+1/2,*z*−1/2; (iii) *x*−1/2,−*y*+1/2,−*z*+1/2; (iv) −*x*+1,*y*+1/2,−*z*+1
Symmetry codes for 110−300 °C: (i) −*x*+1/2,−*y*,*z*−1/2; (ii) −*x*+1/2,*y*+1/2,*z*−1/2 (iii) −*x*+1,−*y*,−*z*; (iv) −*x*+3/2,−*y*,*z*−1/2; (v) *x*−1/2,*y*,−*z*+1/2; (vi) −*x*+3/2,*y*+1/2,*z*−1/2; (vii) *x*,−*y*+1/2,*z*
Symmetry codes for 400 °C: (i) −*x*+1/2,−*y*,*z*−1/2; (ii) −*x*+1/2,*y*+1/2,*z*−1/2; (iii) −*x*+1,−*y*,−*z*; (iv) −*x*+3/2,−*y*,*z*−1/2; (v) *x*−1/2,*y*,−*z*+1/2; (vi) −*x*+3/2,*y*+1/2,*z*−1/2; (vii) −*x*+1,*y*+1/2,−*z*+1; (viii) −*x*+1,−*y*,−*z*+1; (ix) *x*,−*y*+1/2,*z*

Table S34. B−O bond lengths in the $Ag_3B_6O_{10}I$ structure.

Bond	25 °C	110 °C	120 °C	140 °C	300 °C	400 °C
B1−O3^{i}	1.375(3)	1.353(8)	1.365(8)	1.373(7)	1.370(8)	1.363(7)
B1−O5	1.359(3)	1.374(8)	1.361(8)	1.364(7)	1.357(9)	1.352(7)
B1−O6^{i}	1.360(3)	1.361(9)	1.357(9)	1.354(8)	1.359(9)	1.353(8)
B2−O1	1.472(3)	1.458(9)	1.464(9)	1.455(8)	1.453(9)	1.458(8)
B2−O4	1.509(3)	1.535(7)	1.530(7)	1.522(7)	1.509(8)	1.523(7)
B2−O5^{ii}	1.450(3)	1.418(9)	1.440(9)	1.457(8)	1.467(9)	1.454(8)
B2−O6	1.435(3)	1.444(8)	1.439(8)	1.433(8)	1.427(9)	1.417(7)
B3−O1	1.365(3)	1.360(7)	1.352(7)	1.354(7)	1.361(7)	1.358(6)
B3−O1^{iii}	1.365(3)	1.360(7)	1.352(7)	1.354(7)	1.361(7)	1.358(6)
B3−O2	1.359(5)	1.355(13)	1.356(13)	1.360(12)	1.376(14)	1.376(12)
B4−O2	1.447(5)	1.422(12)	1.438(12)	1.448(11)	1.443(12)	1.440(11)
B4−O3^{iv}	1.459(3)	1.466(7)	1.462(7)	1.454(7)	1.471(7)	1.450(6)
B4−O3^{v}	1.459(3)	1.466(7)	1.462(7)	1.454(7)	1.471(7)	1.450(6)
B4−O4^{iv}	1.529(5)	1.510(12)	1.501(12)	1.506(10)	1.490(12)	1.505(10)

Symmetry codes: (i) $-x+1,-y,-z+1$; (ii) $x+1/2,y,-z+1/2$; (iii) $x,-y-1/2,z$; (iv) $x-1/2,-y-1/2,-z+1/2$; (v) $x-1/2,y,-z+1/2$

Table S35. Selected bond lengths in the $Na_3B_6O_{10}I$ structure.

Bond	Length (Å)	Bond	Length (Å)
Na1−I1	3.1064(3)	B1−O3^{iv}	1.363(2)
Na1−I1^{i}	3.1064(3)	B1−O5	1.358(2)
Na1−O1	2.4646(12)	B1−O6^{xi}	1.374(2)
Na1−O1^{ii}	2.4646(12)	B2−O1	1.465(2)
Na1−O6	2.5675(12)	B2−O3	1.442(2)
Na1−O6^{ii}	2.5675(12)	B2−O4	1.514(2)
Na2−I1	3.3235(3)	B2−O6	1.454(2)
Na2−I1^{iii}	3.3235(3)	B3−O1	1.3724(18)
Na2−O1	2.3397(12)	B3−O1^{vii}	1.3724(18)
Na2−O1^{iv}	2.3397(12)	B3−O2	1.357(3)
Na2−O3	2.9724(13)	B4−O2	1.445(3)
Na2−O3^{iv}	2.9724(13)	B4−O4^{xii}	1.513(3)
Na2−O5	2.5212(13)	B4−O5	1.463(2)
Na2−O5^{iv}	2.5212(13)	B4−O5^{vii}	1.463(2)
Na3−I1^{v}	3.3771(15)		
Na3−I1^{iii}	3.3241(15)		
Na3−O2^{vi}	3.153(3)		
Na3−O3	2.4843(19)		
Na3−O3^{vii}	2.4843(19)		
Na3−O5^{viii}	3.108(2)		
Na3−O5^{ix}	3.108(2)		
Na3−O6^{v}	2.5976(12)		
Na3−O6^{x}	2.5976(12)		

Symmetry codes: (i) $-x+1,y-1/2,-z$; (ii) $-x+1,-y,-z$; (iii) $-x+1,y-1/2,-z+1$; (iv) $-x+1,-y,-z+1$; (v) $-x+3/2,-y,z+1/2$; (vi) $x+1/2,-y-1/2,-z+1/2$; (vii) $x,-y-1/2,z$; (viii) $x+1/2,-y-1/2,-z+3/2$; (ix) $x+1/2,y,-z+3/2$; (x) $-x+3/2,y-1/2,z+1/2$; (xi) $x-1/2,y,-z+1/2$; (xii) $x-1/2,-y-1/2,-z+1/2$.

Table S36. Eigenvalues of the thermal expansion tensor of $Ag_3B_6O_{10}I$.

	δ-$Ag_3B_6O_{10}I$	γ-$Ag_3B_6O_{10}I$	β-$Ag_3B_6O_{10}I$	α-$Ag_3B_6O_{10}I$		
Temperature range	25−80 °C	80−100 °C	104−120 °C	120−250 °C	250−400 °C	400−600 °C
α_a (10^{-6} °C^{-1})	6	3	−5	12	11	27
α_b (10^{-6} °C^{-1})	−12	−16	−4	10	22	18
α_c (10^{-6} °C^{-1})	13	24	−4	−9	−15	9
α_V (10^{-6} °C^{-1})	7	11	−13	13	17	54

Table S37. Average molar ICOHP values for $Ag_3B_6O_{10}I$ obtained from spin-polarized calculations.

bond	bond length (Å)	ICOHP per average bond (eV)	no. of bonds per cell (*n*)	ICOHP per cell (eV)
Ag−I	2.617−5.013	−0.26	24	−6.21
Ag_1−I	2.617	−0.77	8	−6.16
Ag_2−I	2.755	−0.01	4	−0.04
Ag_3−I	4.787	0.00	4	0.00
Ag_4−I	5.013	0.00	8	0.00
Ag−O	2.304−2.645	−0.06	36	2.15

Table S38. X-ray Rietveld refinement of the $Ag_3B_6O_{10}I$ structure.

Chemical formula	$Ag_3B_6O_{10}I$
M_r	675.36
Temperature (°C)	23(2)
Crystal system, space group	Orthorombic, *Pnma*
a (Å), *b* (Å), *c* (Å)	12.756020(71), 9.721124(57), 8.426373(49)
V (Å^3)	1044.894(18)
Z	4
D_x (Mg m^{-3})	4.29
Radiation type	Co Kα
μ (mm^{-1})	13.279
Data collection	
Diffractometer	Rigaku Miniflex II
θ-range	2.5–62.5,
(sin $\theta/\lambda)_{max}$ (Å^{-1})	0.58
Refinement	
	R_{wp} 0.060
	R_p 0.044
	R_{Bragg} 0.033
S	167
No. of parameters	58

Computer program: *RietveldToThensor*[2].

Table S39. Assignment of the vibrational bands observed in the infrared spectra for $Ag_3B_6O_{10}I$.

Raman peaks, cm^{-1}	IR peaks, cm^{-1}	Assignment
344		Ag−I and Ag−O vibrations
437		
557		
602		
650		
693	715	Out of plane bending
	738	modes of [BO_3] and [BO_4]
777	790	
	814	
	840	
	880	[BO_4] asymmetric and
905	927	symmetric stretching
	945	
	995	
1103	1070	[BO_3] asymmetric and
1204	1190	symmetric stretching
	1270	
1311	1300	

E. References

[1] S. N. Volkov, D. O. Charkin, M. Y. Arsent'Ev, A. v. Povolotskiy, S. Y. Stefanovich, V. L. Ugolkov, M. G. Krzhizhanovskaya, V. v. Shilovskikh, R. S. Bubnova, *Inorganic Chemistry* **2020**, *59*, 2655–2658.

[2] R. S. Bubnova, V. A. Firsova, S. N. Volkov, S. K. Filatov, *Glass Physics and Chemistry* **2018**, *44*, 33–40.

[3] Rigaku Oxford Diffraction, CrysAlisPRO Software System, version 1.171.41.104a (2021), Rigaku Corporation, Oxford, UK.

[4] L. Palatinus, G. Chapuis, *Journal of Applied Crystallography* **2007**, *40*, DOI 10.1107/S0021889807029238.

[5] V. Petříček, M. Dušek, L. Palatinus, *Zeitschrift für Kristallographie - Crystalline Materials* **2014**, *229*, DOI 10.1515/zkri-2014-1737.

[6] K. Momma, F. Izumi, *Journal of Applied Crystallography* **2008**, *41*, DOI 10.1107/S0021889808012016.

[7] E. Dowty, (2003). ATOMS. Version 6.1. Shape Software, Kingsport, TN 37663, USA. http://www.shapesoftware.com.

[8] W. F. Kuhs, *Acta Crystallographica Section A Foundations of Crystallography* **1992**, *48*, DOI 10.1107/S0108767391009510.

[9] P. J. Brown, A. G. Fox, E. N. Maslen, M. A. O'Keefe, B. T. M. Willis, in *International Tables for Crystallography*, International Union Of Crystallography, Chester, England, **2006**.

[10] J. M. Soler, E. Artacho, J. D. Gale, A. García, J. Junquera, P. Ordejón, D. Sánchez-Portal, *Journal of Physics: Condensed Matter* **2002**, *14*, DOI 10.1088/0953-8984/14/11/302.

[11] S. J. Clark, M. D. Segall, C. J. Pickard, P. J. Hasnip, M. I. J. Probert, K. Refson, M. C. Payne, *Zeitschrift für Kristallographie - Crystalline Materials* **2005**, *220*, 567–570.

[12] N. Troullier, J. L. Martins, *Physical Review B* **1991**, *43*, DOI 10.1103/PhysRevB.43.1993.

[13] B. G. Pfrommer, M. Côté, S. G. Louie, M. L. Cohen, *Journal of Computational Physics* **1997**, *131*, 233–240.

[14] R. Dronskowski, P. E. Bloechl, *The Journal of Physical Chemistry* **1993**, *97*, 8617–8624.

[15] V. A. Blatov, A. P. Shevchenko, D. M. Proserpio, *Crystal Growth & Design* **2014**, *14*, 3576–3586.

[16] A. P. Shevchenko, V. A. Blatov, *Structural Chemistry* **2021**, *32*, 507–519.

[17] V. A. Blatov, E. V. Alexandrov, A. P. Shevchenko, in *Comprehensive Coordination Chemistry III*, Elsevier, **2021**, pp. 389–412.

[18] V. A. Blatov, O. Delgado-Friedrichs, M. O'Keeffe, D. M. Proserpio, *Acta Crystallographica Section A Foundations of Crystallography* **2007**, *63*, 418–425.

[19] V. A. Blatov, A. P. Shevchenko, D. M. Proserpio, *Crystal Growth & Design* **2014**, *14*, 3576–3586.

[20] N. ANUROVA, V. BLATOV, G. ILYUSHIN, O. BLATOVA, A. IVANOVSCHITZ, L. DEMYANETS, *Solid State Ionics* **2008**, *179*, 2248–2254.

[21] S. S. Fedotov, A. A. Kabanov, N. A. Kabanova, V. A. Blatov, A. Zhugayevych, A. M. Abakumov, N. R. Khasanova, E. v. Antipov, *The Journal of Physical Chemistry C* **2017**, *121*, 3194–3202.

[22] V. A. Blatov, G. D. Ilyushin, O. A. Blatova, N. A. Anurova, A. K. Ivanov-Schits, L. N. Dem'yanets, *Acta Crystallographica Section B Structural Science* **2006**, *62*, 1010–1018.

[23] V. A. Blatov, A. P. Shevchenko, *Acta Crystallographica Section A Foundations of Crystallography* **2003**, *59*, 34–44.

[24] M. Sale, M. Avdeev, *Journal of Applied Crystallography* **2012**, *45*, 1054–1056.

[25] I. D. Brown, *Chemical Reviews* **2009**, *109*, 6858–6919.

[26] P. Giannozzi, S. Baroni, N. Bonini, M. Calandra, R. Car, C. Cavazzoni, D. Ceresoli, G. L. Chiarotti, M. Cococcioni, I. Dabo, A. Dal Corso, S. de Gironcoli, S. Fabris, G. Fratesi, R. Gebauer, U. Gerstmann, C. Gougoussis, A. Kokalj, M. Lazzeri, L. Martin-Samos, N. Marzari, F. Mauri, R. Mazzarello, S. Paolini, A. Pasquarello, L. Paulatto, C. Sbraccia, S. Scandolo, G. Sclauzero, A. P. Seitsonen, A. Smogunov, P. Umari, R. M. Wentzcovitch, *Journal of Physics: Condensed Matter* **2009**, *21*, 395502.

[27] V. A. Blatov *, *Crystallography Reviews* **2004**, *10*, 249–318.

[28] I. A. Baburin, V. A. Blatov, *Acta Crystallographica Section B Structural Science* **2004**, *60*, 447–452.

[29] P. Barpanda, G. Oyama, S. Nishimura, S.-C. Chung, A. Yamada, *Nature Communications* **2014**, *5*, 4358.

[30] E. v. Antipov, N. R. Khasanova, S. S. Fedotov, *IUCrJ* **2015**, *2*, 85–94.

[31] G. Chiodelli, G. Flor, A. Magistris, G. Campari Vigano', M. Villa, *Journal of Thermal Analysis* **1983**, *28*, 273–278.

[32] Bruker, APEX3, SAINT-Plus and SADABS, Bruker AXS Inc., Madison, Wisconsin, USA, 2016 (n.d.).